ABSTRACT

BAKSHI, SAURABH SANJEEV. Cell Characterization Using High Frequency Ultrasound. (Under the direction of Dr.Xiaoning Jiang.)

Cell characterization has acquired increasing attention and significance as one of the key steps in tissue engineering and genetic study. This thesis presents a new method of characterizing human stem cells quantitatively and in real-time, by establishing a well-studied relationship between the electric impedance of a piezoelectric transducer and the acoustic properties of the matching layer. In this case, the matching layer is represented by the stem cell layer, and the cell acoustic impedance is thus obtained by measuring the electric impedance of the piezoelectric resonator on which the cells were grown and chemically induced to undergo osteogenic differentiation. Experiments were conducted with human adipose derive stem cells (hASC) growing on lead magnesium niobate-lead titanate (PMN-PT) resonator plates under in-vitro conditions. A clear change in the electrical impedance of the piezoelectric transducer was observed over a period of 14 days, during which the cells began to deposit calcium, causing a change in the resonator acoustic load. This observed phenomenon is simulated mathematically by the use of a Mason model for transducer design. A MATLAB program was developed based on the Mason equivalent circuit for a piezoelectric resonator behaving under loaded conditions. Cell thickness, sound speed and densities were required as input parameters for running simulations. These were obtained by conducting pulse-echo experiments on the cell layer growing separately in culture wells using a 50 MHz piezoelectric transducer. The simulation was able to show similar resonator behavior as observed from the impedance experiments. This work is thus an initial step in developing a new technique for characterizing cells based on their mechanoacoustic properties.

Cell Characterization Using High Frequency Ultrasound

by
Saurabh Sanjeev Bakshi

A thesis submitted to the Graduate Faculty of
North Carolina State University
in partial fulfillment of the
requirements for the degree of
Master of Science

Mechanical Engineering

Raleigh, North Carolina

2012

APPROVED BY:

_____	_____
Dr. Fuh-Gwo Yuan	Dr. Jingyan Dong
_____	_____
Dr. Elizabeth Loboa	Dr. Xiaoning Jiang Chair of Advisory Committee

DEDICATION

This work is dedicated to *Mothiai, Mamma, Kailu,* Dad
and my friends *Shrikant* and *Yatin.*

"All that is gold does not glitter,
not all those who wander are lost;

The old that is strong does not wither,

deep roots are not reached by the frost.

From the ashes a fire shall be woken,

A light from the shadows shall spring;

Renewed shall be blade that was broken,

the crownless again shall be king."

~ J.R.R Tolkien

BIOGRAPHY

Saurabh Bakshi was born on May 18, 1987 in Pune, India (literally 'City of Virtue'), the Oxford of the East. He completed his schooling at Symbiosis School, one of the top educational institutes in India. He graduated from AISSMS COE, Pune University, in October 2009 with a Bachelor of Engineering (B.E.) degree. His major was mechanical engineering.

Saurabh had always shown good aptitude in both life sciences and technology. His interest in biology was the result of a mentally nurturing atmosphere fed by his parents, both being top-tier doctors in his hometown. In Fall 2009, Saurabh enrolled as a graduate student in the Department of Mechanical & Aerospace Engineering at North Carolina State University in Raleigh, NC. He started working with Dr. Xiaoning Jiang in the Micro/Nano Engineering Lab in Spring 2010. His research involves the study of human cells from a mechanobiological point of view, thereby tying together both his academic interest areas.

ACKNOWLEDGEMENTS

I would like to express my gratitude to my advisor, Dr. Jiang, whose guidance and motivation played a crucial role in the successful completion of this research, along with the accomplishment of my Master's degree. I am thankful for the ample patience and faith he demonstrated in me, as well as for all the opportunities he gave me. It has been a pleasure working with him and I am indebted for his support. I would like to thank Dr. Loboa for her valuable advice and for allowing me to use the facilities in the CML Lab. I am also grateful to Dr. F.G. Yuan, Dr. Dong and Dr. Loboa for serving as members of my advisory committee and providing valuable insight and suggestions.

My labmates, Kim, Laura, Wenbin, Gio, Jianguo and Sijia made my stay in the Lab (our home-away-from-home) enjoyable. I am happy to have made such great friends who encouraged me to do well. I am thankful for the patience shown by the students in the CML lab. I would like to thank Pattie and John especially for agreeing to stay back in the lab and allowing me to work at the most odd hours.

I also thank my friends and roommates in Raleigh, Matar, Hashim, BeeDee, Pacman, Bulla, Bulgeet and Moka for all their love and support over the past two years. It was because of their emotional support that I was able to stay away from my family.

I would not have reached this point without the love and encouragement of my mother and grandmother.

TABLE OF CONTENTS

LIST OF TABLES

LIST OF FIGURES

Chapter 1

INTRODUCTION

Cell characterization has achieved elevated significance in the fields of gene therapy and tissue engineering [1-4]. It is important to identify cell properties and study their behavior as they are used to regenerate new tissue. Human stems cells exhibit pluripotent nature and have great potential in a wide range of regenerative medical applications. Cell characterization is also useful to study cell mechanisms and their response to different conditions [5]. An understanding of the mechanical characteristics of undifferentiated stem cells can greatly aid research investigating the forces necessary to promote differentiation into various cell lineages [6]. Previous work has demonstrated that malignant cells exhibit different material properties than benign cells [7]. Study of single-cell biomechanics has led to new findings in the progression of diseases like malaria [8]. Therefore, cell mechanical properties can be used to identify and isolate cancer cells [9]. It has been found that human cells exhibit extensive variability in their chemical and mechanobiological response due to donor-to-donor variability; thus, cell characterization can enable identification of proper biological procedures. Some commonly used cell characterization techniques in practice consist of optical and acoustic microscopy, tactile sensors at the micro/nano scale and atomic force microscopy [10]. Active research has been focused on eliminating the limitations of biological incompatibility, cost, time consumption, size and complexity.

1.1 Literature Review

A review of existing cell characterization methods, their operation principle, advantages and limitations, is given below. Broadly, cell characterization techniques are classified as contact and non-contact type methods. Figure 1 shows the important characterization techniques in use with biological samples.

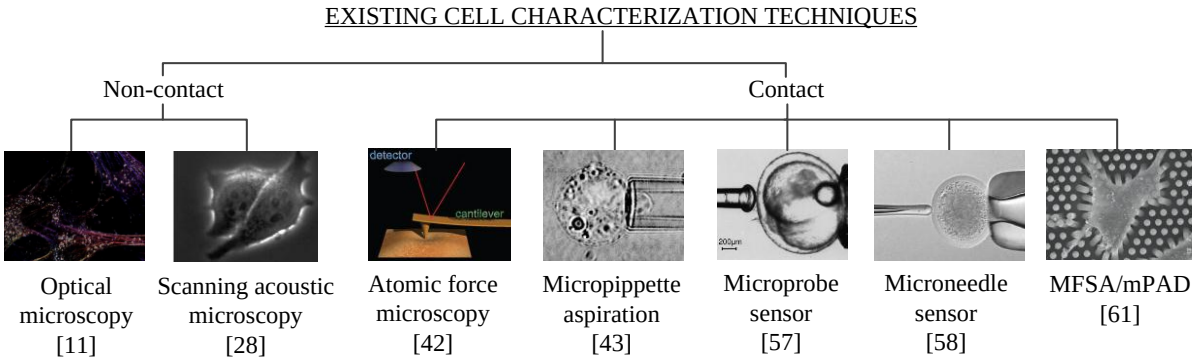

Figure 1: Different cell characterization methods in current use

1.1.1 Non-contact Methods

Optical microscopy is probably the oldest non-contact technique in use to characterize cells. Cells are observed under an optical microscope, and visible cell features are used to identify cell types. Optical imaging techniques can provide very good contrast, but have limited penetration depth in tissues due to high optical scattering [11]. Optical microscopy, however, has the biggest disadvantage that it needs the cells to be stained and fixed. Chemical fixatives are used to preserve tissue from degradation, and to maintain the structure of the cell and of sub-cellular components (nucleus, endoplasmic reticulum, mitochondria). These fixatives preserve tissues or cells mainly by irreversibly cross-linking proteins. This process, while preserving the structural integrity of the cells and tissue, can damage the biological functionality of proteins, particularly enzymes, and can also denature them to a certain extent. This can be detrimental to certain histological techniques. It is challenging to achieve good contrast by local difference in refraction and/or transmission spectrum. Cell staining is a technique that can be used to better visualize cells and cell components under a microscope. Cells are stained to enhance visualization of the cell or certain cellular components under a microscope. Cells may also be stained to highlight metabolic processes or to differentiate between live and dead cells in a sample. Most stains can be used on fixed or non-living cells, while only some can be used on living cells. Staining is done by chemicals, and the tissue, after being stained, often completely loses its biological functions.

The other non-contact technique developed extensively in the last 50 years is acoustic microscopy, where an ultrasound transducer is used to image the specimen [12-15] or

measure its mechanical properties [16-28]. Analysis is carried out based on the principles of time-resolved acoustic microscopy for measuring velocity of sound in the medium, and spectroscopy is applied for determining elasticity, acoustic impedance and physical dimensions. Acoustic microscopy is used as one of the following: Scanning Acoustic Microscope (SAM), Scanning Laser Acoustic Microscope (SLAM) or C-mode Scanning Acoustic Microscope (C-SAM). Acoustic scanning microscopy in the GHz range has been developed for imaging of single cells *in vivo* [29]. Although acoustic microscopy does not involve any chemical process of the cells, the equipment is bulky and expensive. It requires analysis and image processing, which makes it a lengthy procedure even for imaging a single cell. There is also the limitation of axial resolution, and only thinly sliced tissue can be studied using acoustic microscopy.

Photoacoustic or optoacoustic imaging is a new hybrid method that combines the advantages of optical and acoustical techniques [30]. In this minimally invasive imaging method, the tissue volume is illuminated by a laser source which causes heating and thermal expansion of the tissue. This heating process is accompanied by the generation of acoustic waves as a result of the thermal displacements. These acoustic waves are less sensitive to scattering compared to the optical field, and are used to obtain data from the exposed region [31]. Another such combined high-resolution multiphoton-acoustic scanning microscopy method was developed by Shenkl *et al* [32, 33]. A review of the existing and recently developed biomicroscopy techniques is given by Foster *et al* [34].

Recently, imaging of cells based on measurement of acoustic impedance of the cells has been demonstrated [35]. The research team at Tohoku University, Japan, used an impedance microscope to demonstrate the change in acoustic impedance of a HIFU-exposed chicken breast muscle [36]. Nakano *et al.* also used impedance microscopy to image cells cultures *in vitro* [37]. Raum *et al.* used acoustic impedance mapping along with computed tomography mapping to measure the elastic stiffness coefficient (c_{33}) of human bone [38].

Another optical technique involves trapping and stretching of cells using optical tweezers [39] or a laser source [40]. It has also been developed as an acoustic technique [41].

1.1.2 Contact Methods

Contact methods for measuring cell properties include the use of micro tactile sensors (MTS) and micro devices like micro-pipettes, micro-plates and micro-needles. Optical or magnetic tweezers and magnetic twisting cytometry are used to mechanically deform the cells and measure their response [42]. The most commonly used technique however, is atomic force microscopy (AFM). An review of the various micro and nano-scale testing techniques for measuring mechanical properties at the cellular level is given in [43].

The tip of an AFM is used to indent soft samples, and the force versus indentation measurement provides mechanical information about the cell sample [44, 45]. It is well established that the AFM can be used to image living cells under physiological conditions in a non-destructive manner [46-48]. AFM can also be used to study material properties [49, 50] by analyzing force curves over a point on the sample surface. A force curve is a plot of the force applied to the AFM tip as the sample is approached and pushed against the tip. In principle, this plot gives the force required to achieve a certain depth of indentation (deformation) from which viscoelastic parameters can be determined. This technique has been used to examine micromechanical properties of a wide range of biological samples: bones [51], platelets [52], bacteria and cancer cells [53]. By collecting arrays of force curves, so-called force volumes, high-resolution 2-D maps of mechanical properties can be produced.

Micro-pipette aspiration technique is used to measure viscoelastic coefficients and adhesion forces of hepatocellular carcinoma cells in mice [54]. Micro-plates are used to compress cells, and the deformation of the pre-calibrated plates as a response to cell stiffness and elasticity is measured [55]. Cells are stretched, compressed or rotated by twisting embedded particles or particles attached to the cell surface using magnetic fields. This method, called magnetic cytometry, is described in [56]. Micro tactile sensors (MTS) shaped as micro-probes and micro-needles [57] have been developed for measuring the stiffness of microscopic materials like ovum [58]. The sensor consists of a piezoelectric element that is divided into vibrating (actuator) and detecting (sensor) components. The resonance frequency of the sensor shifts relative to the stiffness of the contacted material.

Contact methods disturb the cell and alter its natural progression. They might also cause cellular damage and death. These techniques work on a single cell at a time, and need extreme control and accuracy, which makes them highly time consuming.

Recent micro/nano techniques include devices like micro Post Array Detectors (mPADS) [59-61] and Micro-post Force Sensor Arrays (MFSA) [62]. When a cell resides on an array of micro-posts, it bends them at the top. Each force sensing unit can detect the cell traction force at the site where it contacts the cell. Once the lateral deflections of the micro-posts are obtained by image acquisition and analysis, cell traction forces can be determined based on the beam theory. However, this method requires the fabrication of intricate array substrates to grow cells.

The key features, advantages and limitations of the more commonly used cell characterization methods are summarized in Table 1.

Table 1: Comparison of advantages and limitations of existing cell characterization methods

	Use	Biocompatibility	Real-time monitoring	Modular	Ease of use	Fabrication	Cost
Optical microscopy	Imaging technique, cell properties cannot be measured accurately	No; samples need to be stained using chemicals for contrast, which usually kills the cells	No; staining procedure renders the cell sample biologically dead	No; the optical microscope is bulky	Staining cells needs expertise. Using microscope for imaging purposes is relatively simple	No fabrication involved	Fairly expensive
Acoustic microscopy	Used for both imaging and mechanical property measurement	Yes; does not need staining, and it is a non-contact method	Yes; although measurements need to be taken at intervals	No; equipment is bulky	Using an acoustic microscope needs moderate training	No fabrication involved	Moderately expensive
MTS	No imaging , mechanical properties measured by tactile sensing	Yes; but may disturb cells and cause damage/ death	No; process is very sensitive and delicate	No; needs optical microscope system for display	Difficult to use, needs precision and control	Micro-probes and sensors need to be fabricated	Moderately expensive
AFM	Used for both imaging and mechanical property measurement	Yes; but may disturb cells and cause damage/ death	No; process is very sensitive and delicate	No; equipment for control is bulky	Difficult to use, needs precision and control	Micro-probes and sensors need to be fabricated	Moderately expensive
mPADS/MFSA	No imaging, cell traction forces measured	Yes; cells are made to grow freely on fabricated substrate	Yes; data is taken automatically as cells continue to grow	Yes; only device is the fabricated micro-substrate	Simple to use, not much processing involved	Micro-substrate is expensive to fabricate	Not expensive

1.2 Motivation

From the literature review, it is known that the existing methods to characterize cells are static, expensive, time-consuming, and sometimes destructive. Hence, there is a need for an accurate, repeatable cell characterization technique that can track cell property change in real-time and can detect an anomaly in a high throughput manner. Human stem cells possess great potential in a variety of regenerative applications. A good understanding of stem cell mechanics at the single cell level may provide information about the role of biophysical forces affecting differentiation. In this study, a method of cell detection and characterization based on the electrical impedance of a piezoelectric transducer as a function of cell acoustic properties is proposed. Electrical impedance has not been previously investigated as a quantitative criterion for cell characterization. The previous techniques used impedance microscopy techniques for cell characterization. The specimen sample was imaged using sound speed and impedance mapping carried out by using an ultrasound microscope. These impediography processes were time consuming and required a complex SAM system to map the samples. The proposed method is non-contact, free from use of destructive staining procedures, and does not require any complicated system. Results are instantaneous and real-time monitoring of cells has been demonstrated. Specifically, human adipose derived stem cells (hASC) were grown on lead magnesium niobate-lead titanate (PMN-PT) piezoelectric resonator plates acting as the substrate, and the change in resonator electric impedance was measured. This change was attributed to the change in material properties of the hASC layer. A pulse-echo experiment was carried out to evaluate hASC layer acoustic impedance, which was used as an input parameter in a computational simulation model.

1.3 Thesis Overview

This thesis presents a new technique to characterize human stem cells based on their mechanoacoustic properties. The idea is explained in theory and further demonstrated in working by experimentation. A simulation model based on a proven technique for a parallel

application is applied by making suitable modifications to validate the theory and experimental results.

- In Chapter 2, the basic concepts that are applied in impedance measurement of ultrasound transducers are discussed in detail. The principle applied in this research project is explained with the help of mathematical notation. An equivalent circuit model for a piezoelectric resonator under loaded and unloaded conditions is explained using network theory.
- Chapter 3 comprises of the experimental setup and a description of the actual experiment. Key aspects of the measurement process are explained thoroughly.
- Validation of the observed results from experimentation is done in chapter 4. It is done with the aid of pulse-echo experiment and by writing a simulation program in MATLAB based on the earlier described equivalent circuit.
- Finally, a summary is put together from all the findings observed in this project. Future steps and scope of application are discussed briefly.

Chapter 2

FUNDAMENTALS

The most important component in this technique is the piezoelectric resonator. Piezoelectricity is the property of a material to react as a mechanical deformation to an electric stimulus, or, conversely, react electrically to a mechanical stimulus. A piezoelectric material can be a ceramic, a polymer, or a composite. It has the unique characteristic of generating charge under an applied stress, which is called the direct piezoelectric effect. The inverse piezoelectric effect is the mechanical deformation under an electric field. This bilateral transduction requires the understanding of both mechanical and electrical principles for analysis.

The concept behind the proposed technique is inspired by the principles used in the design of piezoelectric ultrasound transducers. An ultrasound transducer consists of an active element which is basically a piezoelectric resonator, one or more matching layers and a backing layer, all of which are enclosed in a housing. The significance of each is explained below. In the characterization technique developed, the human stem cells were grown on a lead magnesium niobate-lead titanate (PMN-PT) piezoelectric plate. The cell layer can be considered as the matching layer. The resonator behavior then can be well explained by the use of an equivalent circuit model, like the Butterworth-Van Dyke model, the Mason model, the Redwood-Lamb model or the KLM (Krimholtz-Leedoem-Matthaei) model. For this research, the Mason model was implemented for developing a simulation program to validate the observed results.

The aim of this chapter is to thoroughly explain the theory behind the developed characterization method.

2.1 Important Terminology

2.1.1 Acoustic Impedance

Acoustic impedance (Z) is a material property that describes the behavior of a particle when it is exposed to a pressure (sound) wave. It is a measure of the resistance offered by a substance to the propagation of a sound wave through it. It is calculated as

$$Z_0 = \rho v \tag{1}$$

ρ is the density of the substance and v is the speed of sound in the medium.

The above formula is for 'specific' or 'characteristic' acoustic impedance. This is the acoustic impedance of a material per unit cross sectional area, and is an intrinsic material property. For a surface area A, the acoustic impedance is given by

$$Z = \rho v A = Z_0 A \tag{2}$$

2.1.2 Electric Impedance

Electric impedance (Z_{el}) is the measure of the opposition to the passage of a current through an electrical circuit when a voltage is applied. Thus, it is the term analogous to acoustic impedance on the electric port of a piezoelectric resonator. It is defined as the frequency domain ratio of the voltage (V) to the current (I).

2.1.3 Active Material

The active element is the piezoelectric or ferroelectric material that converts electrical energy into mechanical (ultrasonic) energy and vice versa. Polarized ceramics, piezoelectric polymers and composites are the most commonly used active materials.

2.1.4 Matching Layer

The matching layer is the front layer that is in between the active material and the coupling media. It serves as an acoustic transformer between the high acoustic impedance of the active element and the low impedance coupling fluid, which is usually water. The matching layer is usually of quarter-wave ($\lambda/4$) thickness. Usually, the matching layer has acoustic impedance (Z_M) given by

$$(Z_M) = \sqrt{Z_a * Z_w} \quad (3)$$

where Z_a = acoustic impedance of active element

Z_w = acoustic impedance of coupling fluid

2.1.5 Backing Layer

When the active layer is excited, it emits acoustic waves in a direction normal to its surface. As a result, waves are generated in two directions, and those propagating away from the target object may cause interference due to secondary reflections and result in image distortion and generation of artifacts. To avoid this, a highly attenuative, high density material is used to absorb the vibration energy radiating from the back face of the active element. A backing layer is also used to control the spatial pulse length. When the acoustic impedance of the backing layer matches that of the active element, we get a heavily damped transducer that displays good range resolution, but has low signal amplitude. If there is a mismatch in acoustic impedance between the element and the backing, more sound energy will be reflected forward into the test material, and we get a transducer that is lower in resolution but higher in signal amplitude or greater in sensitivity. Usually, a high impedance material like tungsten powder mixed in epoxy is used as the backing material. The thickness of the backing layer is several times that of the piezoelectric component for effective attenuation of energy.

Figure 2 is a schematic representation of the arrangement of each of these layers in a fully functioning device.

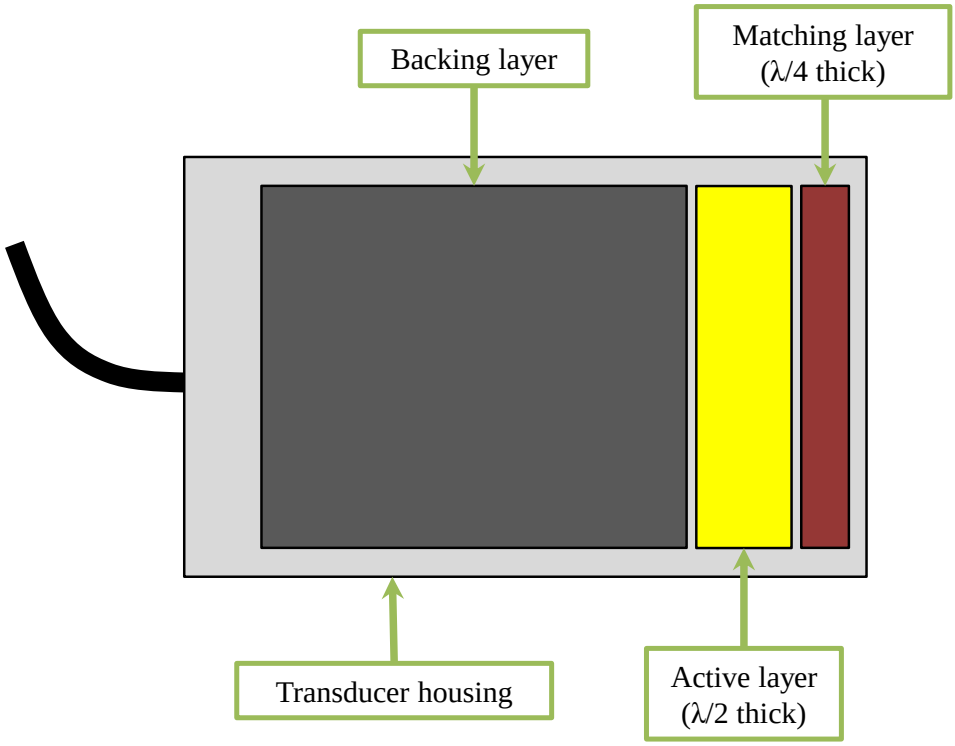

Figure 2: Schematic arrangement of the different layers in a piezoelectric transducer

2.2 Piezoelectric Transduction

The transduction in piezoelectric materials can be explained mathematically with the help of linear relationships between mechanical and electric variables. These expressions, called 'constitutive relations' are as follows:

$$
\begin{aligned}
[T] &= \left[c^{D}\right][S] - [h]^{t}[D] \\
[D] &= \left[\varepsilon^{S}\right][E] + [e][S] \\
[S] &= \left[s^{E}\right][T] + [d]^{t}[E] \\
[D] &= \left[\varepsilon^{T}\right][E] + [d][T] \\
[S] &= \left[s^{D}\right][T] + [g]^{t}[D] \\
[E] &= \left[\beta^{T}\right][D] - [g][T] \\
[T] &= \left[c^{E}\right][S] - [e]^{t}[E] \\
[E] &= \left[\beta^{S}\right][D] - [h][S]
\end{aligned}
\qquad (4)
$$

where β, ε are dielectric constants, d, g, e, h are piezoelectric constants, and s, c are elastic constants. The description of each symbol is given with the units in Table 2.

Table 2: List of terms used in constitutive relations

Symbols	Description	Type	Units
T	Stress	Mechanical	N/m^2
S	Strain	Mechanical	-
E	Electric field strength	Electrical	V/m
D	Electric displacement	Electrical	C/m^2
s	Elastic compliance	Mechanical	m^2/N
c	Elastic stiffness	Mechanical	N/m^2
ε	Permittivity	Electrical	F/m
β	Dielectric impermeability	Electrical	m/F
d	Piezoelectric charge – stress constant	Electromechanical	C/N or m/V
e	Piezoelectric dielectric – stress constant	Electromechanical	C/m^2 or N/Vm
g	Piezoelectric voltage – strain constant	Electromechanical	m^2/C or Vm/N
h	Piezoelectric charge – strain constant	Electromechanical	N/C or V/m

It is important to show the interrelationship between the acoustic load layer acting on a piezoelectric resonator, and the change it induces in the electric impedance of the transducer. This is achieved by the use of a 1-D transducer model [63]. For simplicity purposes, it is assumed that the transducer lateral dimensions are much larger than the thickness and that the transducer performance is linear in nature. All losses are neglected.

The resonator is represented as a three-port device with one electric port and two acoustic ports, one each for the two faces of the resonator. The electric port is represented by the current (I) and voltage (V) applied across the two electrode faces of the resonator. The acoustic ports are represented by the force (F) and particle velocity (v) acting on each surface of the piezoelectric resonator plate.

Consider a 1-D representation of the piezoelectric resonator of length l as shown in Figure 3. For an element of thickness dz the stress T in the piezoelectric medium due to a wave propagating in the z-direction is a function of both time and direction.

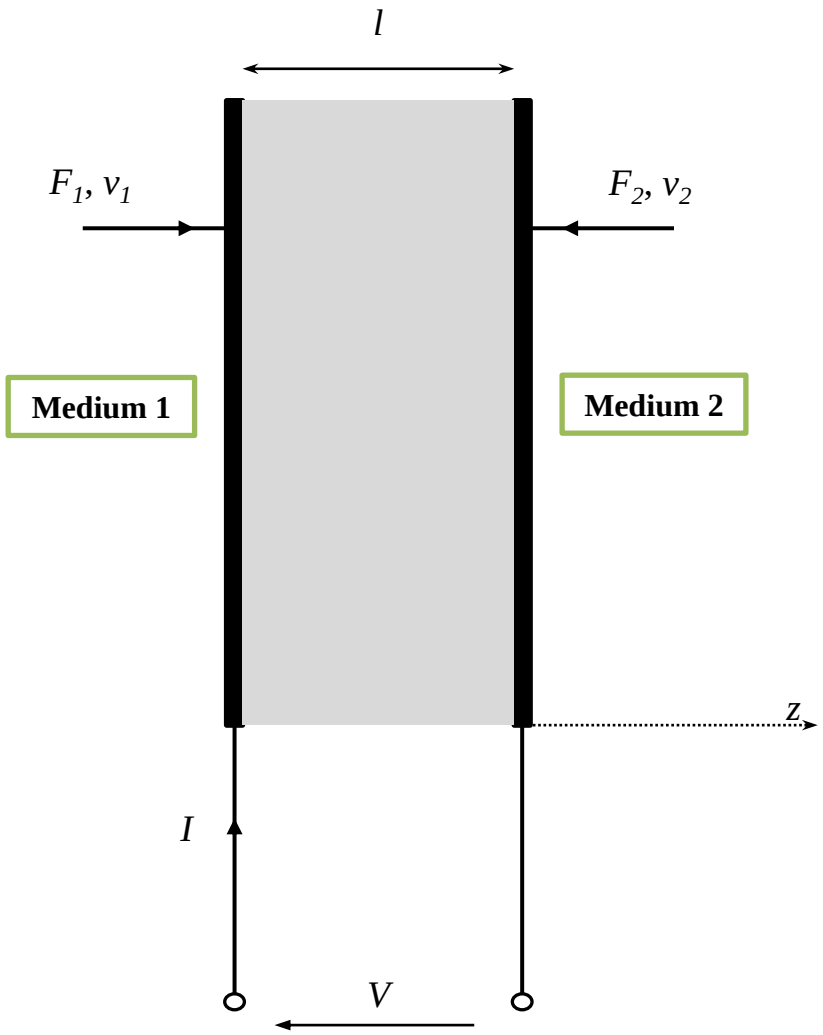

Figure 3: 1-D model of a piezoelectric plate excited in the thickness expansion mode

Denoting displacement of the plane along the z-axis at a given instant of time by ξ, the strain (S) for this elementary volume is given as

$$S \approx \frac{\partial \xi}{\partial z} \tag{5}$$

Assuming that A is the cross sectional area of the elementary volume of thickness dz, the force acting on this volume is given as

$$A(\partial T / \partial z)dz \tag{6}$$

and mass is given by

$$\rho_0 A dz \tag{7}$$

Then from Newton's second law, we have

$$\frac{\partial T}{\partial z} = \rho_0 \frac{\partial^2 \xi}{\partial t^2} \tag{8}$$

Applying the constitutive relationship

$$[T] = \left[c^D\right][S] - [h]^t [D]$$

where c^D = elastic stiffness at constant electric displacement

S = mechanical strain

D = dielectric displacement

h = piezoelectric charge-strain constant

Taking the partial derivative with respect to z, we get

$$\frac{\partial T}{\partial z} = c^D \frac{\partial S}{\partial z} - h \frac{\partial D}{\partial z} \tag{9}$$

In the absence of free charges in the piezoelectric medium, $\partial D / \partial z = 0$

Thus, we get the differential equation for the displacement

$$c^D \frac{\partial^2 \xi}{\partial z^2} = \rho_0 \frac{\partial^2 \xi}{\partial t^2} \tag{10}$$

The equations governing the relationship between the electrical and mechanical properties of the transducer at the three ports are obtained by solving this equation using appropriate boundary conditions.

Denoting wave number by $\beta = \omega / c_0^D = \omega / \sqrt{c^D / \rho_0}$

the relationship between the mechanical and electric terms is expressed in matrix form as

$$\begin{bmatrix} \bar{F}_1 \\ \bar{F}_2 \\ \bar{V} \end{bmatrix} = -i \begin{bmatrix} Z_a \cot(\beta l) & Z_a \cos ec(\beta l) & h/\omega \\ Z_a \cos ec(\beta l) & Z_a \cot(\beta l) & h/\omega \\ h/\omega & h/\omega & 1/(\omega C_0) \end{bmatrix} \begin{bmatrix} \bar{v}_1 \\ \bar{v}_2 \\ \bar{I} \end{bmatrix} \tag{11}$$

Here, F = force acting on resonator face

V = voltage measured across electric terminal

v = sound velocity in medium at face

I = current at electric port

Z_a = resonator acoustic impedance

ω = angular frequency

l = resonator thickness

$h = k\sqrt{c^D/\varepsilon^S}$ is the piezoelectric charge-strain constant

$C_0 = A\varepsilon^S/l$ is the clamped capacitance of the resonator

ε^S is the clamped dielectric permittivity of the piezoelectric element (constant strain)

2.3 Equivalent Circuit for a Piezoelectric Crystal

In 1948, Mason proposed the circuit model shown below [64] with terminal equations similar to those given by equation (11). The equivalent circuit shown in Figure 4 known as Mason's equivalent circuit is used in the design and analysis of piezoelectric transducers [65-67]. The operation of the proposed technique can be explained by expounding the theory of piezoelectric transducer design. The Mason model separates the piezoelectric material into an electric port and two acoustic ports through the use of an ideal electromechanical transformer.

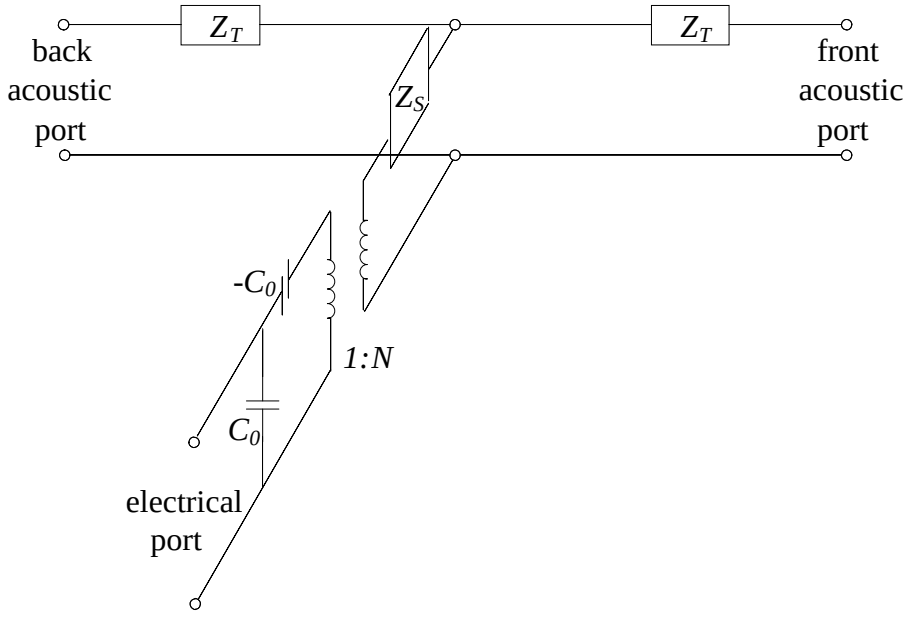

Figure 4: The Mason equivalent circuit for a free (unloaded) piezoelectric transducer

The center branch is the electrical port where voltage is applied or produced and the left and right branches are the acoustic ports, i.e., the transducer surfaces that either transmit or receive mechanical stress. Thus a voltage transformed to the acoustic side of the transducer becomes a force. On the electric side, the relation $V = Z_e I$ holds, where Z_e is the electrical impedance; while on the acoustic side, force is related to velocity v through $F = Z_a v$ where Z_a is the acoustic impedance given by equation (2). Thus, it is possible to express mechanoacoustic parameters as electric terms by using network theory.

For a thickness mode resonator, the Mason model is expressed mathematically as:

$$Z_T = iZ_a \tan(\frac{\omega l}{2v^D}) \tag{12}$$

$$Z_S = -iZ_a \cos ec(\frac{\omega l}{v^D}) \tag{13}$$

where Z_T is the acoustic impedance at the front and back ports of the transducer, Z_S is the impedance of the voltage source, ω is the resonant frequency, l is resonator thickness, A is resonator cross section area, v^D is stiffened compressional speed, ε^S is the clamped permittivity, C_0 is clamped capacitance for transducer ($C_0 = A\varepsilon^S/l$).

The electrical impedance measured at the electrical port for a free resonator is given by

$$Z_{el} = Z_C(1 - \frac{Z_C N^2}{Z_A}) \tag{14}$$

where $Z_C = \frac{1}{i\omega C_0}$

$Z_A = Z_S + \frac{Z_T}{2}$

$N = C_0 h$ is the turns ratio for transformer

$h = k\sqrt{c^D/\varepsilon^S}$, c^D is the elastic stiffness

k is the complex electromechanical coupling coefficient ($k^2 = e^2/c^D\varepsilon^S$)

2.4 Layered Model

The acoustic load layer is modeled based on the application of equations similar to those used for the piezoelectric element. The representation is shown as Figure 5.

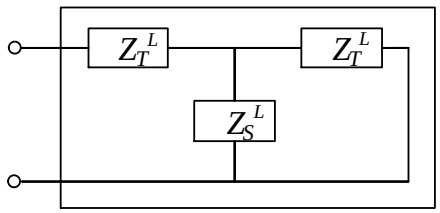

Figure 5: The Mason circuit representation for an acoustic load layer

Applying equations. (12) and (13), we have for the acoustic load layer

$$Z_T^L = iZ_A^L \tan(\omega l^L / 2v^L) \tag{15}$$

$$Z_S^L = -iZ_A^L \cos ec(\omega l^L / v^L) \tag{16}$$

where the superscript L stands for the 'load layer'.

For simplification of explanation, only one of the acoustic ports of the Mason equivalent circuit is connected to one acoustic port of an acoustic element. The other acoustic port of both, the equivalent circuit, and the acoustic load layer, are shorted.

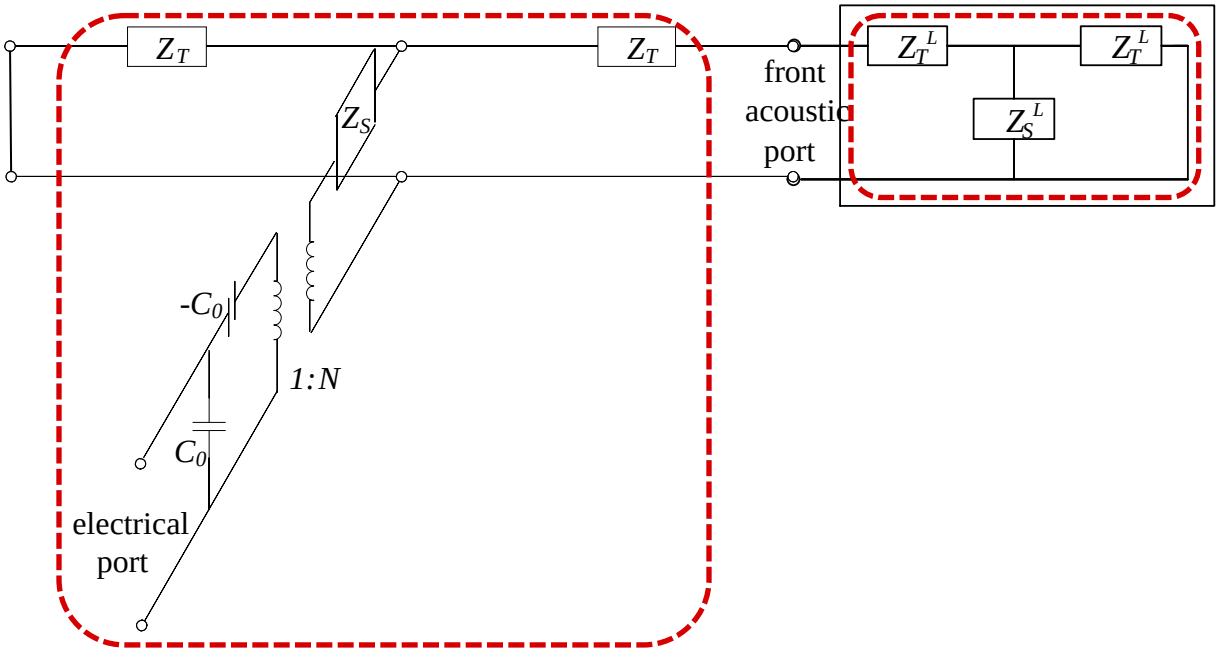

Figure 6: The Mason equivalent circuit for a piezoelectric transducer with an acoustic load on one surface and shorted (unloaded) on the other

Total layer impedance

$$Z_L = Z_T^L + \frac{Z_T^L Z_S^L}{(Z_T^L + Z_S^L)}$$

$$= -iZ_A^L \tan(\frac{\omega l^L}{v^L}) \quad (17)$$

Acoustic (mechanical) impedance for combined resonator and load layer

$$Z_A = Z_S + \frac{Z_T(Z_T + Z_L)}{2Z_T + Z_L} \quad (18)$$

The transmitted electric impedance observed at the electric port of the transducer is given by equation (14) using the value of Z_A obtained from equation. (18).

A similar approach is followed to evaluate the electric impedance for a resonator with acoustic loads at the front and back ports. Resonator behavior for change in mechanical properties of the hASC layer was simulated in MATLAB to observe the change in resonator electric impedance as the cells underwent osteogenic differentiation. A pulse-echo experiment was carried out to obtain cell thickness and sound speed data, which were necessary input parameters for the model. The experimental procedure and the results observed from the experiment are discussed in Chapter 3, followed by a comparison with the simulation results and the pulse-echo experiment in Chapter 4.

Chapter 3

MEASUREMENT TECHNIQUE

This chapter describes the experimental procedure and the setup used for the same. The resonator electric impedance was the characterizing property for this experiment. Chapter 2 describes the dependence of electric impedance on the acoustic impedance of the front load in transducer design theory. The same principle was used and thereby, a change in the cell layer acting as the front load for a PMN-PT resonator was detected.

3.1 Resonator Preparation

Four PMN-PT thickness mode resonators of dimensions 10 mm × 10 mm × 0.45 mm (L × W × t) were used for measuring the change in acoustic impedance of the hASC layer. These resonator plates had a gold electrode of thickness ~ 35 nm deposited on each 10mm × 10 mm surface. A coaxial wire (38 AWG, Hitachi Cable Manchester) of length 80 mm was bonded to each electrode of the four resonator plates. The wires were bonded using conductive silver epoxy (MG Chemicals). A minimum amount of epoxy was used to avoid any damping effect on the resonator sensitivity. The epoxy was cured at room temperature for 8 hours. A picture of a wire-bonded PMN-PT resonator plate prior to seeding cells is shown in Figure 7.

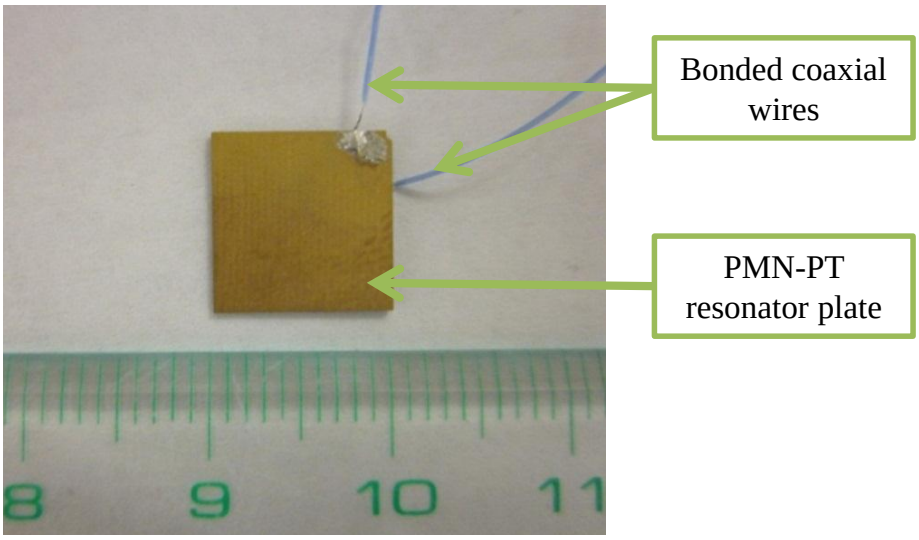

Figure 7: Picture of a PMN-PT thickness mode resonator plate with coaxial wires

3.2 Cell Culture and Differentiation

Human adipose derived stem cells (hASC) were cultured in complete growth medium (CGM) - Eagle's Minimum Essential Medium, alpha-modified (α-MEM) [68] supplemented with 10% fetal bovine serum, 2 mM L-glutamine, 100 units/mL penicillin, and 100 μg/mL penicillin/streptomycin.

A preliminary test was performed to verify that the chemicals in the epoxy used to bond the wire electrodes did not have any harmful effect on the cell culture once the epoxy was cured. The gold electrode substrate was found to be suitable for cell growth. The plates were sterilized by immersing them in 70% EtOH (ethanol-water solution) for a day before seeding the cells. An image of the resonator plate with cells growing directly on the gold electrode is shown in Figure 8. Additionally, cells were also seeded in thirty Falcon tissue culture dishes of 35 mm diameter. The cells seeded on the resonator plates were monitored for change in the resonator electric impedance, which was measured using an impedance analyzer. The cell cultures seeded on the polystyrene substrate of the Falcon dishes were used for measuring cell thickness and the speed of sound in the cell medium. This data was used along with the mathematical model to simulate the resonator behavior and validate the observed impedance change.

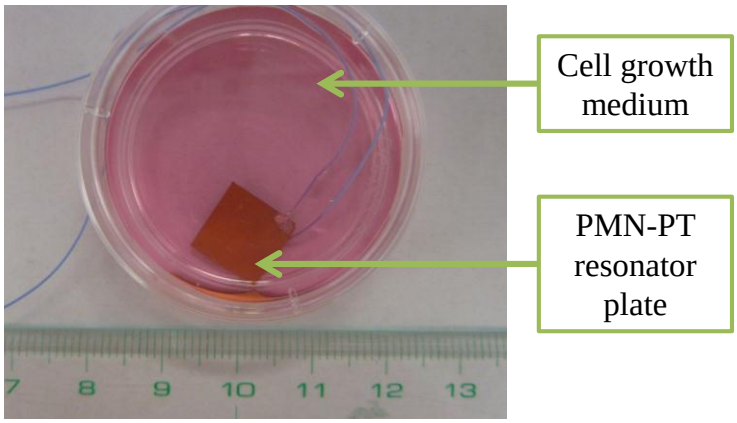

Figure 8: Cells growing in α-MEM on a PMN-PT resonator plate

The incubator for the culture wells was maintained at 100% humidity and 37 °C with a 95% air and 5% CO_2 atmosphere. A confluency of 80% was observed on day 4 by inverted microscopy, after which the medium was changed in half the culture wells to osteogenic differentiation medium (ODM) - complete growth medium supplemented with 50 μM ascorbic acid, 0.1 μM dexamethasone, and 10 mM β-glycerolphosphate. Cell confluency is a measure of the number of the cells in the cell culture dish, and refers to the coverage of the dish by the cells. Thus, the cells growing on two of the resonator plates and fifteen of the Falcon dishes started differentiating into osteogenic cells. The remaining two resonator plate cell samples and cell cultures in fifteen Falcon dishes were maintained in complete growth medium. The culture medium in all the wells was replaced with the corresponding growth media type every three days to replenish the nutrients absorbed by the cells.

3.3 Experimental Setup

The PMN-PT resonator electric impedance was measured as a signature of monitoring change in stem cell mechanical properties. Figure 9 shows a photograph of the experiment and a schematic for the experiment procedure is shown in Figure 10.

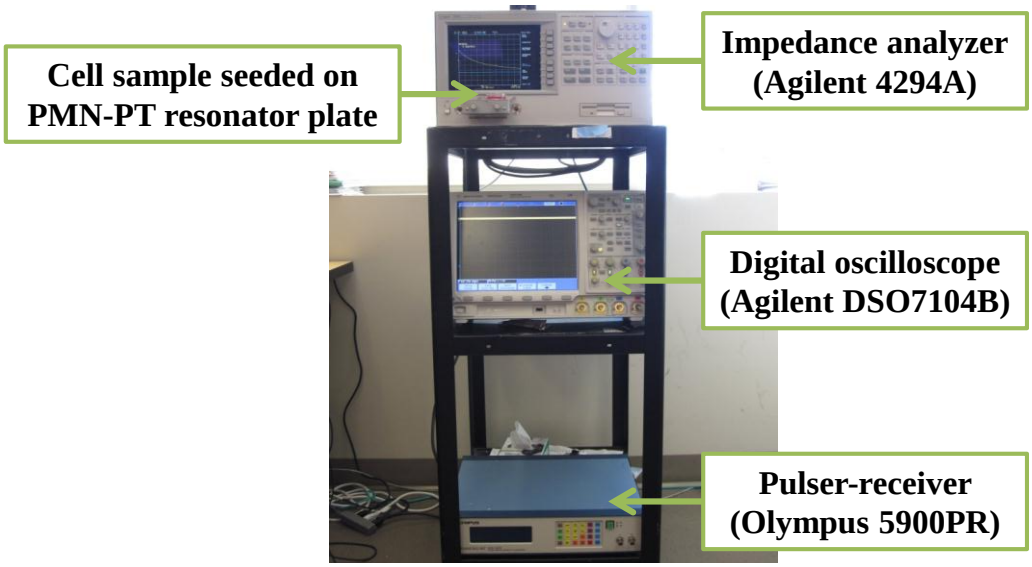

Figure 9: Setup of impedance measurement experiment

The schematic diagram explains procedures for both impedance measurement and the pulse-echo experiment for validation using a simulation model. This chapter deals only with the impedance measurement portion of the experiment. The pulse-echo test is discussed in Chapter 4.

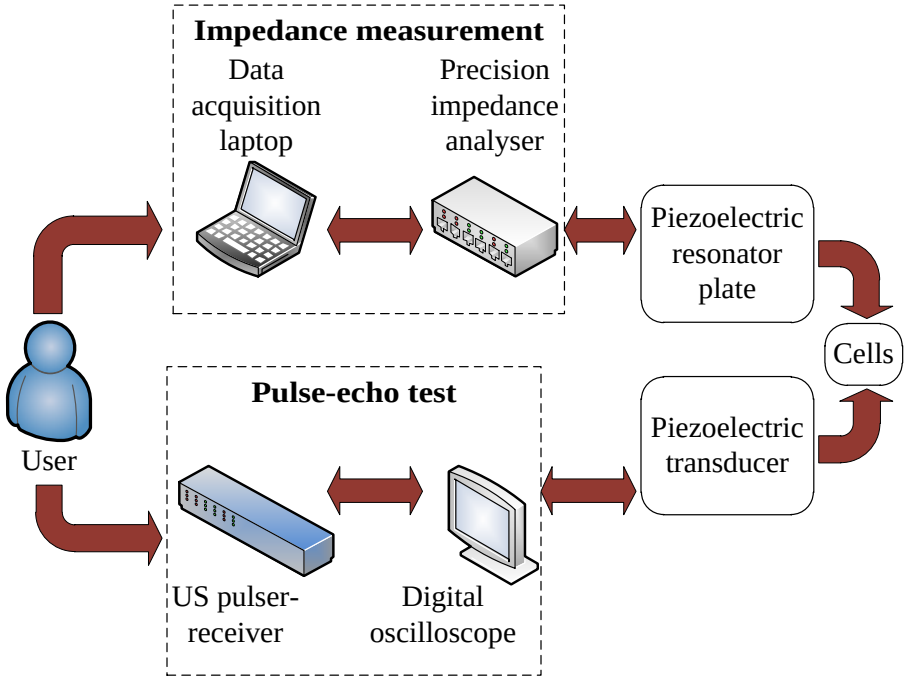

Figure 10: Schematic of experimental procedure

The resonator electrical impedance was tracked as stem cells were seeded directly on PMN-PT thickness mode resonator plates. Cell properties including cell density, speed of sound in the cell, wave attenuation and other mechanical and acoustic characteristics change as the cells undergo osteogenic differentiation. This cell layer growing on the resonator surface can be assumed as an acoustic load layer acting at one acoustic port of the resonator. The other acoustic port is exposed to the cell growth medium, and has no acoustic load acting on it. From the resonator behavior described earlier in Chapter 2, it is evident that any change in the acoustic load layer properties will result in a change in the electrical impedance measured across the electric port of the resonator. Thus, as the cell layer continues to change into osteogenic cells and deposit calcium, a change in the resonator impedance is expected in the measurements taken every day for a period of 14 days.

The resonator electric impedance was measured by using a precision impedance analyzer (Agilent 4294A). The impedance analyzer was calibrated for use with the fixture (16047E) for ‘open’ and ‘short’ configurations each time measurements were taken to eliminate measurement errors. A photograph of the impedance analyzer under operation is shown as Figure 11.

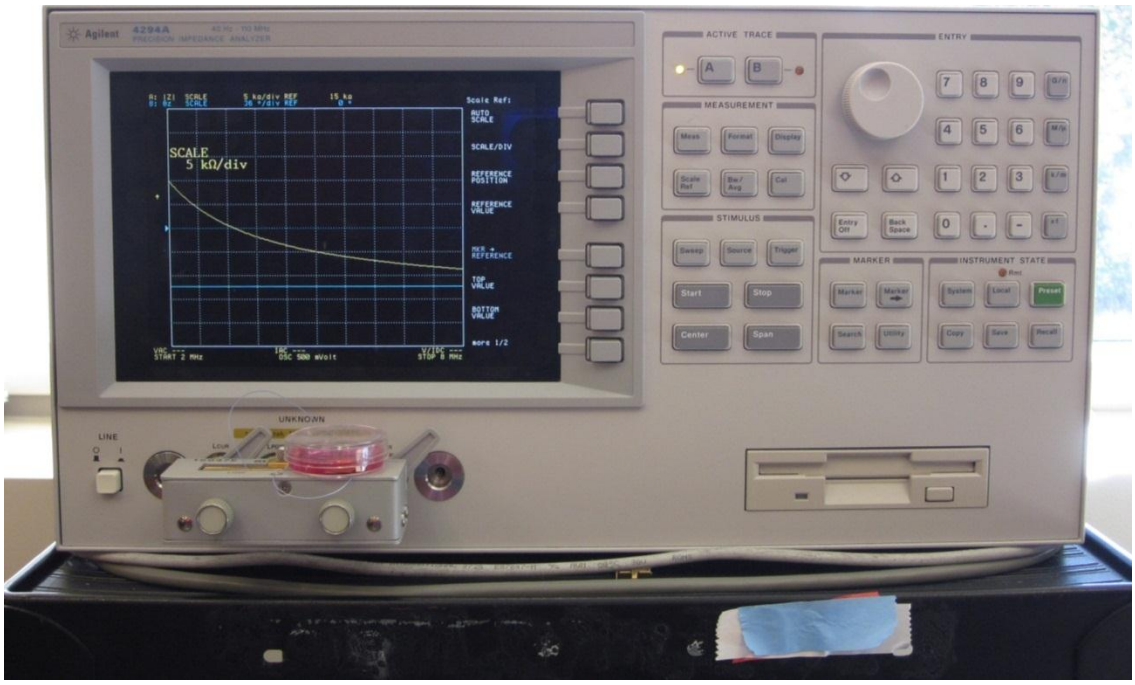

Figure 11: Setup of impedance measurement experiment

All measurements were taken with the culture wells placed inside a laminar flow chamber to keep the entire process sterile. The resonator plate with stem cells growing on it was connected to the two terminals of the impedance analyzer using the free ends of the two coaxial wires bonded to each electrode of the resonator. The PMN-PT resonator was kept immersed in the cell growth medium while all measurements were taken. Measurements were taken with the help of an Excel Macro program (Agilent Inc.). All measurements were saved using a GPIB interface between a data acquisition laptop and the impedance analyzer.

To eliminate the effect of noise, each resonator was measured twice for its electrical impedance and phase. The values for each day were then averaged for analysis. Also, there were two resonators with non-differentiating cell samples, and two with differentiating cell samples. This averaging gave a more uniform set of data points and removed any inconsistencies.

Every day, for a period of 14 days, the electric impedance at resonance and anti-resonance frequencies was recorded for the four piezoelectric plates. The resonance and anti-resonance frequencies were also noted.

3.4 Results and Discussion

It has been shown earlier that increased mass loading of piezoelectric resonators causes an increase in the electrical impedance at resonant frequency and a decrease in the impedance value at anti-resonant frequency [65, 69]. The electrical impedance for the differentiating cells increased at a steeper rate as compared to that for the CGM cells with the culture time at resonant frequency. Conversely, the electrical impedance measured at the anti-resonant frequency decreased faster for the differentiating cells than the CGM non-differentiating cells from day 1 to day 14. The change in the resonator electric impedance for the osteogenic differentiating cells measured at resonant and anti-resonant frequencies can be seen in Figure 12.

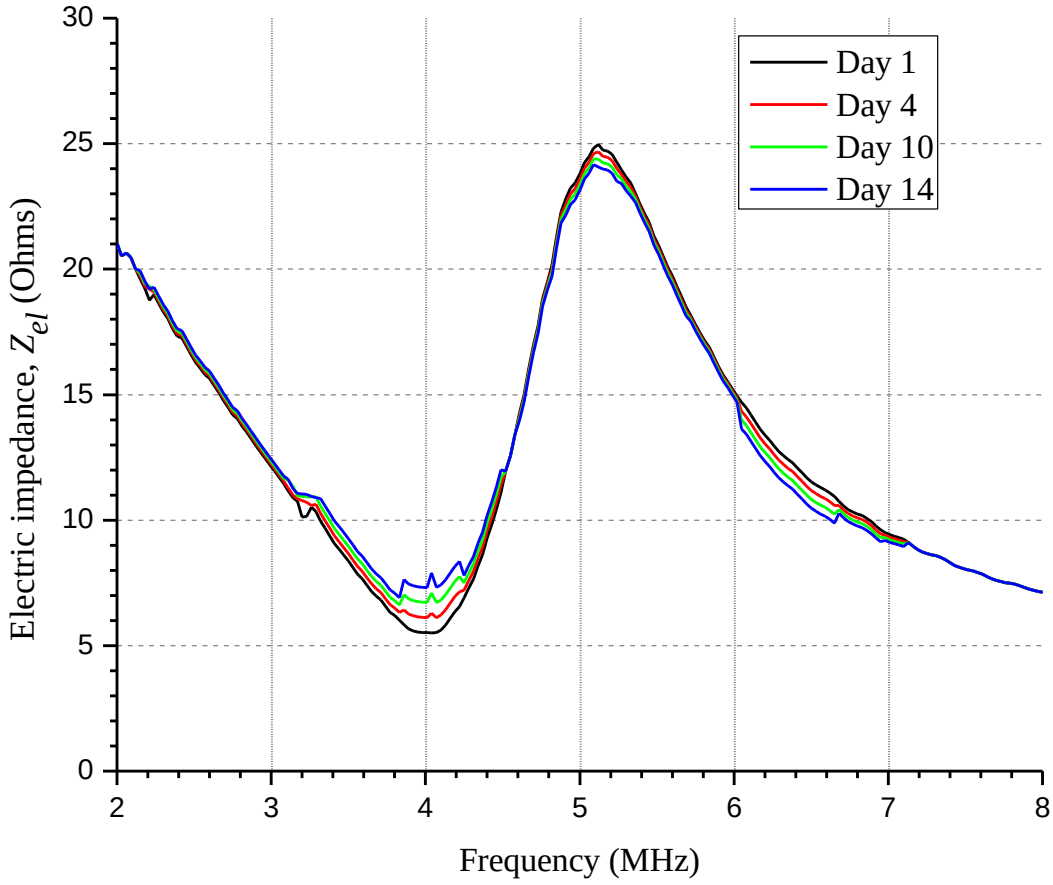

Figure 12: Measured change in resonator electrical impedance for the differentiating cells

The acoustic impedance of a material is a function of the speed of sound in the material, and its density. As hASC underwent osteogenic differentiation and accreted calcium, the cell layer thickness and density increased relative to the non-differentiating cells. The differentiating cell layer consisted of calcium accretion zones, in addition to the cell adhesion sites. Human ASC in complete growth media has a specific density of almost unity (the same as the medium) [68], while calcium has a known specific density of 1.55. The pulse-echo experiment indicated a steeper rise in sound speed for the osteogenically differentiating cells compared to the non-differentiating samples over the period of 14 days. As both, the speed of sound and the density of the differentiating cell layer increased gradually by the end of 14 days, the acoustic impedance increased, as explained by equation (1).

As explained earlier in Chapter 2, the resonator electric impedance is a function of the acoustic impedance of load layer, and thus the observed increase in resonator electric impedance is proportional to the increase in the acoustic impedance.

It was also observed that the non-differentiating cells registered an increase in the acoustic impedance value. This might be explained by the fact that the cell layer, although it did not undergo osteogenic differentiation, tried to achieve 100% confluency as the cells kept growing and multiplying. This resulted in an increase in the cell surface area. Acoustic impedance is directly proportional to the surface area of the load layer, as given by equation (2). In addition, although the hASC were selected for this experiment because they tend to adhere to the substrate as a monolayer of cells, some overlap occurs after confluence is reached. This results in an increase in the cell layer thickness, which affects the speed of sound. Thus, the change in the impedance value for the non-differentiating cells is valid. The change in the resonator electric impedance for the non-differentiating cells is shown in Figure 13.

From Figure 12 and Figure 13 , it was observed that the change in the resonator electrical impedance value is also accompanied by a shift in the resonance and anti-resonance frequencies for both the differentiating and non-differentiating cell samples. This shift is very small, and is neglected in this study. It can however be explained as the effect of the damping caused by the cell layer as the cells multiply and occupy the entire surface of the resonator. For the differentiating samples, the frequency shift is also a result of the change in cell layer mass due to calcium accretion. However, this increase in mass due to both, cell growth and calcium deposition, is extremely miniscule, and hence the frequency shift was ignored.

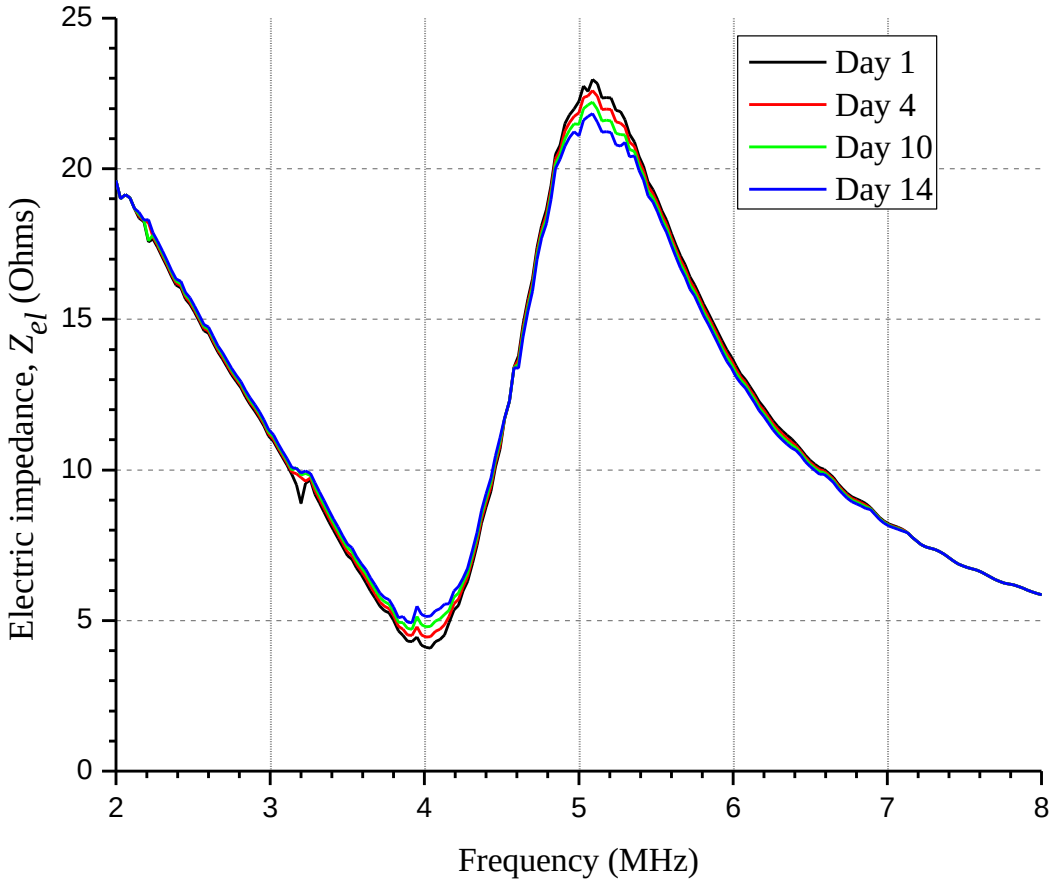

Figure 13: Measured change in resonator electrical impedance for the non-differentiating cells

To ensure that the measured electrical impedance difference between the osteogenic differentiated cells and the undifferentiated stem cells was an accurate representation of the changing cell properties and differentiation process, and not because of the different growth media used with the respective cells, measurements were taken in the respective differentiation medium. No statistical differences in medium impedance were found.

A comparison of the change in the normalized impedance at the resonant frequency of 4 MHz for hASC cultured in CGM and ODM is shown in Figure 14.

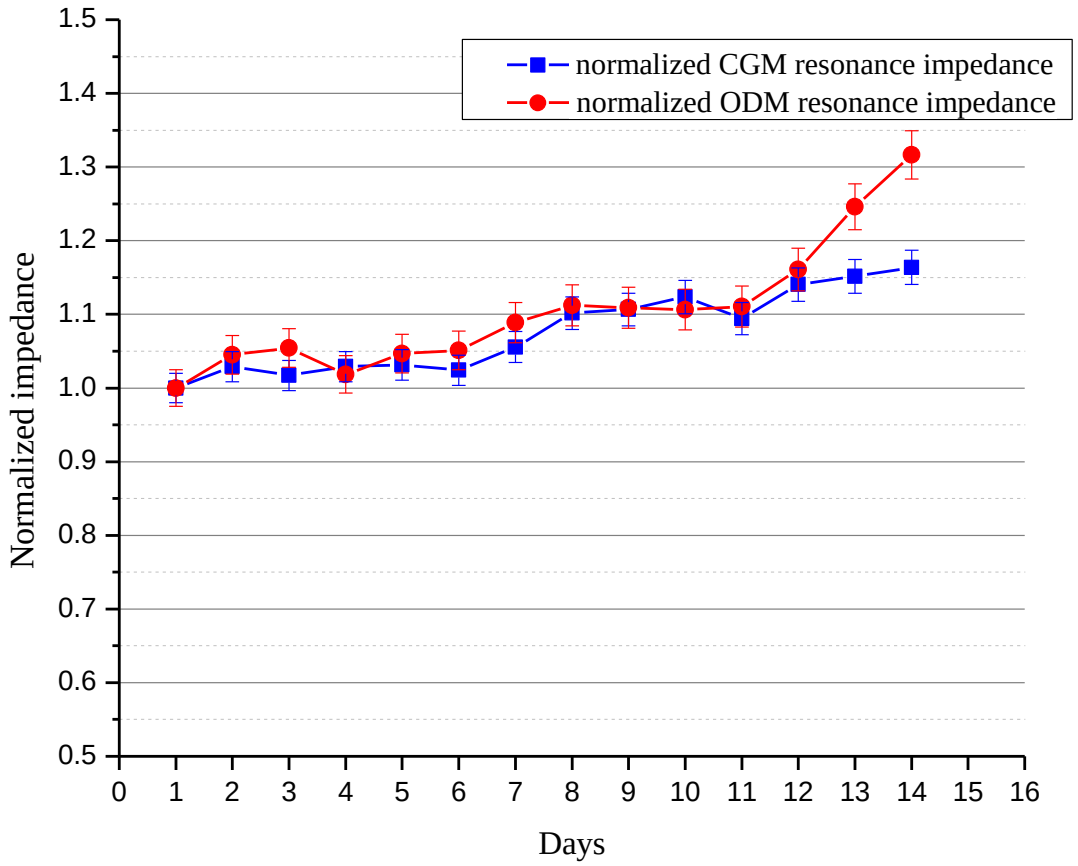

Figure 14: Change in resonance electrical impedance for hASC cultured in complete growth medium (CGM) and in osteogenic differentiation medium (ODM) tracked over a period of 14 days

As stated earlier the cell growth media was changed on day 4 and subsequently changed after every 3 days. Replacing the cell growth media was characterized by a sharp change in impedance which is partly attributed to a change in pH, temperature, and dissolved CO_2, but is primarily a cell response to the media change [70]. The measured data was averaged by conducting simultaneous impedance measurements with hASC samples growing on two PMN-PT resonators for each of the CGM and ODM groups. The calculated variation within each group was smaller than the variation between the two groups. The 5% error bars shown in Figure 14 indicate that although the absolute impedance change for the differentiating cells was small, it is still significant as a means to characterize the osteogenic differentiating cells from the non-differentiating cells.

Table 3 summarizes the measured resonator electrical impedance change for the differentiating and the non-differentiating cell samples.

Table 3: Resonator electrical impedance values measured by the impedance analyzer

	Osteogenic differentiating sample (ODM)		**Non-differentiating sample (CGM)**	
Impedance change (%) $(\frac{Z_{sample} - Z_{medium}}{Z_{medium}})$	**At resonance frequency**	**At anti-resonance frequency**	**At resonance frequency**	**At anti-resonance frequency**
	31.7	-7.32	13.46	-3.52

3.5 Histological Examination

Both hASC maintained in complete growth medium (CGM) and osteogenic differentiation medium (ODM) were fixed and stained using Alizarin Red after 14 days, to visualize cell mediated calcium accretion. This is used as an indicator of osteogenic differentiation of the hASC. Calcium forms an Alizarin red S-calcium complex in a chelation process. The reaction is birefringent. The samples were imaged under an optical microscope (Olympus STM6) and are shown in Figure 15.

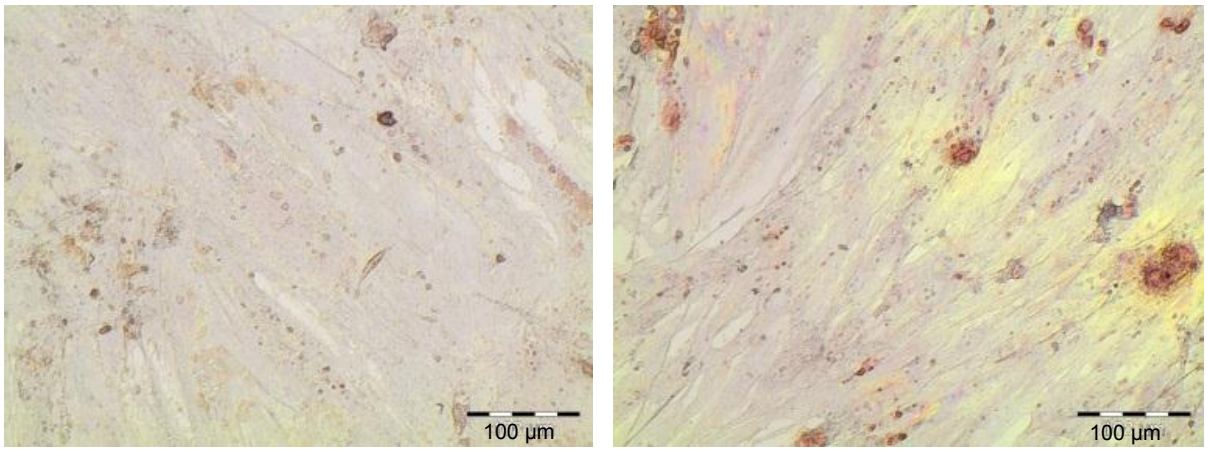

Figure 15: Cells observed at 10x magnification at the end of 15 days of seeding. (a) Cells growing in non-differentiating complete growth media (CGM). (b) Cell-mediated calcium accretion for hASC cultured in osteogenic differentiated medium (ODM). The red spots are areas of calcium concentration

From the images of stained hASC cultured in CGM and ODM in Figure 15, it can be seen that calcium accretion was not excessive. This can explain the small change in observed resonator impedance. However, we would expect resonator impedance to increase more with greater calcium accretion.

A steady trend in resonator impedance tracking can be seen in Figure 14. This implies that the cells were growing and proliferating in a healthy fashion, and were not affected by the experiment or the daily measurement process.

Chapter 4

VALIDATION BY SIMULATION

The change in resonator electric impedance recorded as described in Chapter 3 can be calculated with the use of a mathematical model for the resonator behavior. Based on the Mason equivalent circuit for a piezoelectric resonator, a simulation program was developed in MATLAB. The cell sound velocity and cell density were the required input parameters for the model. The speed of sound in the cell layer can be determined by performing a pulse-echo test on the cell sample. This chapter describes the pulse-echo experiment setup and the subsequent validation procedure for the observed impedance change.

4.1 Pulse-echo Method

The speed of sound is associated with the scattering and attenuating behavior of the propagation medium and is therefore an important acoustic parameter for quantitative characterization of cells. The pulse-echo test is the most commonly used technique for non-destructive evaluation (NDE) and ultrasonic testing of materials. Any ultrasound experiment requires a coupling fluid between the transducer and the specimen for the propagation of the ultrasonic waves. The presence of a defect or a feature having acoustic impedance other than that of the specimen is indicated by the reception of an echo signal before that of the back wall echo. Usually, a CRT screen or an oscilloscope is calibrated to show the separation in distance between the arrival time of an echo signal as against that of the back wall echo of the specimen. This enables the precise calculation of the sample thickness and the speed of sound in the specimen. A schematic of a typical pulse-echo test setup is shown in Figure 16.

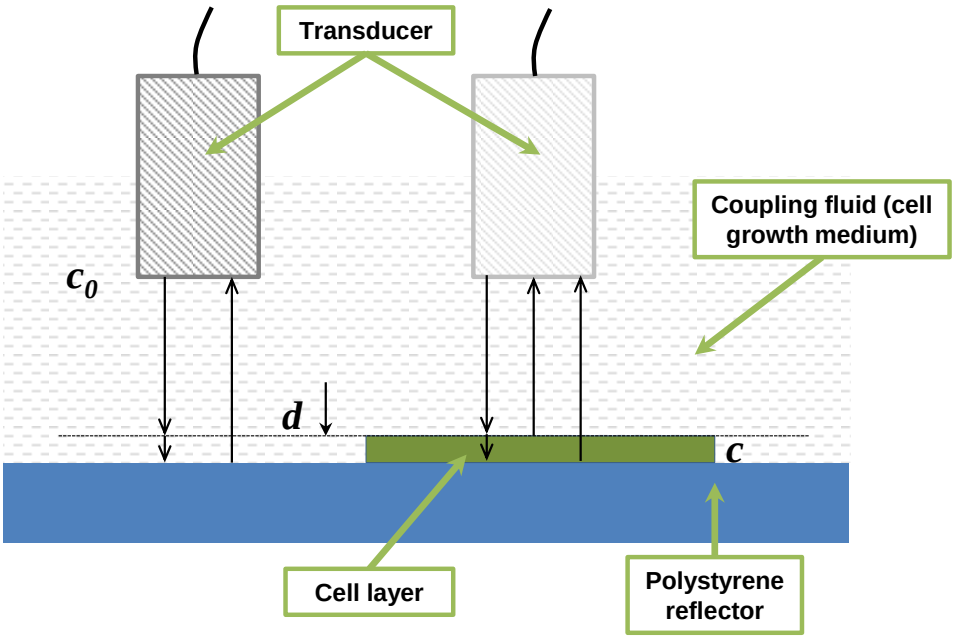

Figure 16: Principle of pulse-echo test

The analysis of the above experiment can be done in either time domain, or in frequency domain. Measurement of the travel time is complicated by waveform distortion due to the tissue inhomogeneity and the roughness of interface, which reduces the accuracy of the measurement [71]. Moreover, for calculating the thickness of a cell layer with thickness in the range of 5-15 μm, the time lag between the reflections from the top and bottom surfaces is difficult to estimate because the cell thickness is less than or very close to the wavelength of the acoustic wave. At such small thicknesses, the reflections from the top and bottom surfaces may overlap each other. Also, the speed of sound in the cell layer is almost the same as that of the coupling medium surrounding it, and the echo from the cell surface is hardly visible compared to that from the reflector surface. Hence, phase analysis in the frequency domain is usually preferred.

A frequency scan of the specimen is required for thickness measurement in the frequency domain, and it takes a long time to scan the frequency as well as to mechanically scan the sample. The setup cost is expensive. In addition, it is not easy to realize high stability of the measured data. As a result, a method in which time domain signal was converted into the

frequency domain for further analysis was adopted [72]. Sound speed and thickness were both calculated by phase analysis of the Fourier transformed echo signal.

4.2 Time–frequency Analysis Method

As shown in Figure 16, consider a cell layer of thickness *d* placed on a rigid reflecting substrate like polystyrene. The cell culture was kept immersed in the cell growth medium, which also acts as the coupling fluid for the transmission of acoustic waves from the transducer into the cell layer. Let c_0 be the speed of sound in the coupling medium. A transducer with a suitable frequency in the range of 50-100 MHz, high enough to be able to acoustically resolve the cell layer of thickness in the micron scale, was held parallel to the reflecting surface at the focal distance of the ultrasound transducer.

The transducer was excited by a low intensity pulse to avoid damaging the cells. The input pulse was set at a high frequency repetition rate to achieve an almost-continuous output. The transducer is operated in pulse-mode since the same transducer is operated as both transmitter and receiver, and using it in continuous-mode may cause overlap and interference of the transmitted and reflected waves. Accordingly, reflection of ultrasound waves occurred at the front and back faces of the specimen and at the rigid reflector surface.

The wave reflected from the top and bottom surfaces of the cell layer contains an oscillating component. Hence, this waveform was subjected to deconvolution processing by the reference signal. The two reflections were separated in the time domain and were analyzed in the frequency domain to determine the sound speed [73]. The reference signal consists of the waveform obtained by the reflection of sound from the polystyrene substrate where no cells were present. This allows the separation of the reflections at the front and rear sides of the cell layer. The analysis procedure is explained with the help of Figure 17.

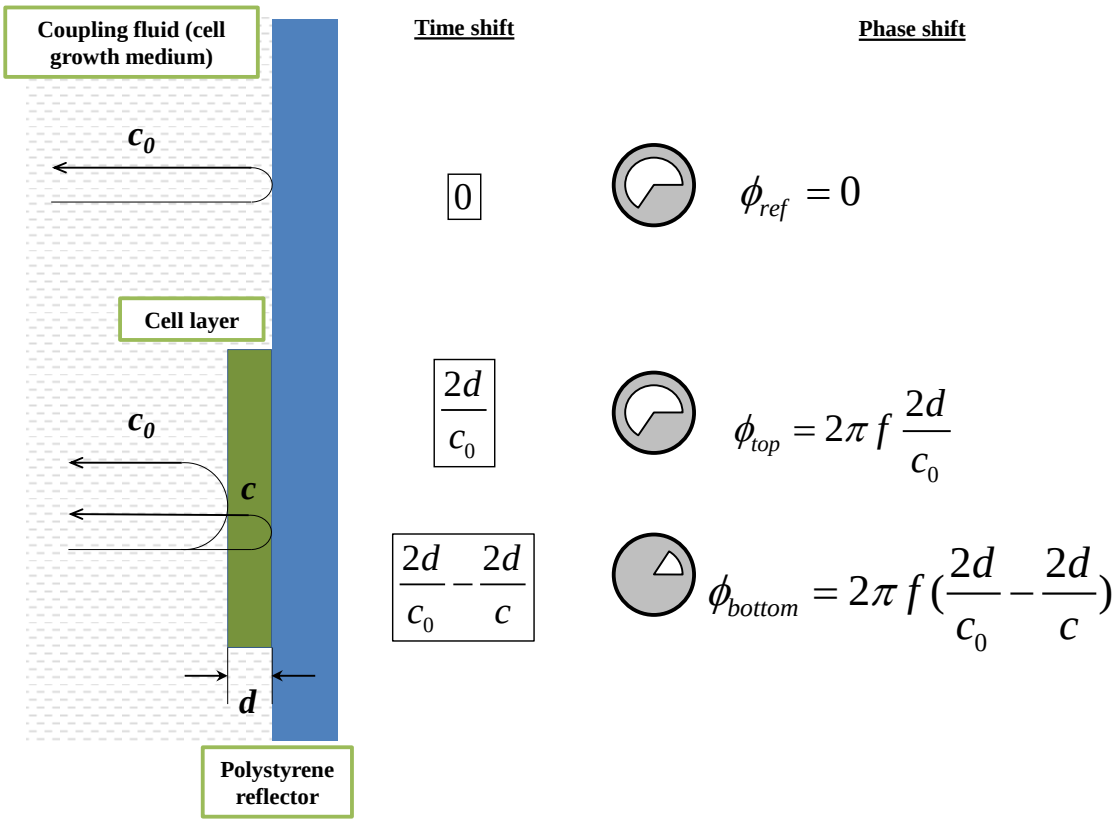

Figure 17: Introduction of time and phase shift in the reflected waveform due the to cell layer

The intensity and phase spectra of these separated waveforms were calculated by Fourier transforming the waveform. The spectrum of each separated waveform was normalized by that of the reference waveform.

The cell layer gives us a shift of $\frac{2d}{c_0} - \frac{2d}{c}$ in the time domain,

which corresponds to a phase shift of $2\pi f (\frac{2d}{c_0} - \frac{2d}{c})$ in the frequency domain.

This is the phase shift obtained from the wave reflected from the bottom of the cell layer. The maximum intensity point on the normalized intensity spectrum shown in Figure 22 corresponds to the reflection from the top of the cell layer, while the minimum point corresponds to the reflection from the bottom of the cell layer. Then for any minimum frequency *f*, if we know the phase angle *Φ* at that frequency, the cell layer thickness *d* and sound speed *c* are given by equations (19) and (20), respectively.

$$d = \frac{c_0}{4\pi f}\phi_{top} \tag{19}$$

$$c = \left(\frac{1}{c_0} - \frac{\phi_{bottom}}{4\pi fd}\right)^{-1} \tag{20}$$

4.3 Experimental Setup

A photograph of the test setup used for performing the pulse-echo experiment is shown below in Figure 18. A 50 MHz LNO (lithium niobate) ultrasound transducer was used for the test (USC UTRC). The measured transducer characteristics are given in Table 4.

Table 4: Ultrasound transducer properties

Aperture diameter (mm)	Focal length (mm)	Bandwidth (%)	Sensitivity (dB)	Axial resolution (μm)
2	5	48	-36	0.3

The instrumentation for the pulse-echo test consisted of a pulser-receiver (Olympus 5800PR) and a digital oscilloscope (Agilent DSO7104B). An input pulse of magnitude 1 μJ was generated at a pulse repetition frequency (PRF) of 200 MHz by the pulser-receiver. The transducer was driven by this input signal. The pulser-receiver input parameters were set as shown in Table 5.

Table 5: Input parameters for the pulse-echo test

PRF (Hz)	Energy (μj)	Damping (Ohms)	HP filter (MHz)	LP filter (MHz)	Attenuation (dB)	Gain (dB)	RF output phase
200	1	50	10	100	5	54	0º

The cell cultures in the Falcon polystyrene well were exposed to the acoustic wave. Input pulse and received echo signal were monitored by using a digital oscilloscope (Agilent DSO7104B). The bandwidth and sampling rate were 1 GHz and 4GSa/s respectively. A XYZ manual linear stage (Newport 460A-XYZ stage with three SM-13 actuators), with a resolution of 1 μm was used to position the transducer relative to cells. FFT analysis of the

received signal was carried out for calculating sound speed and thickness data for further use in the simulation model.

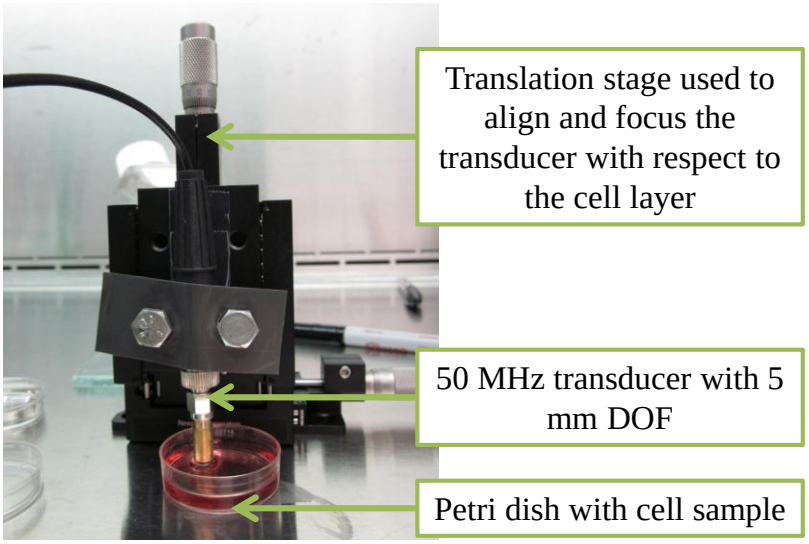

Figure 18: Setup of pulse-echo experiment

4.4 Analysis of Data

Figure 19 is the waveform of the ultrasound wave reflected from the polystyrene substrate without the presence of any cells. Figure 20 shows the waveform obtained from the pulse echo experiment due to the introduction of a cell layer between the transducer and the substrate. Both the figures are a function of reflection voltage (V) plotted versus a time scale (μs) as the x-axis. These waveforms are for the differentiating cells grown in the polystyrene wells obtained on day 14 of the experiment. The small reflection seen as the highlighted portion in the waveform in Figure 20 denotes the reflection from the cell layer. The two reflections from the cells and the substrate interfere to a large extent, making it very difficult to determine the time lag between the two waveforms. The cell layer thickness thus cannot be calculated by analysis in the time domain.

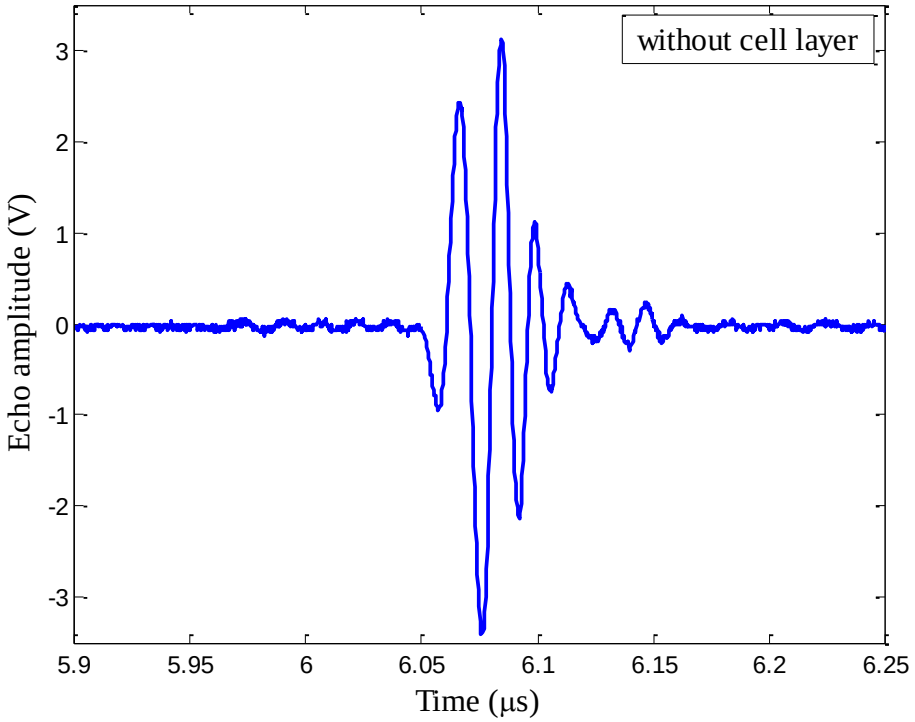

Figure 19: Waveform of wave reflected from polystyrene substrate without the presence of cells

We can calculate the velocity of sound c_0 in the cell growth medium because we know the distance traveled by the acoustic wave as it travels to and from the substrate. The distance d traveled by the wave is the same as the focal length of the transducer, which was set using the XYZ stage. The time taken for the wave to travel is half of that recorded in the echo waveform. The value of c_0 was calculated as 1531 m/s.

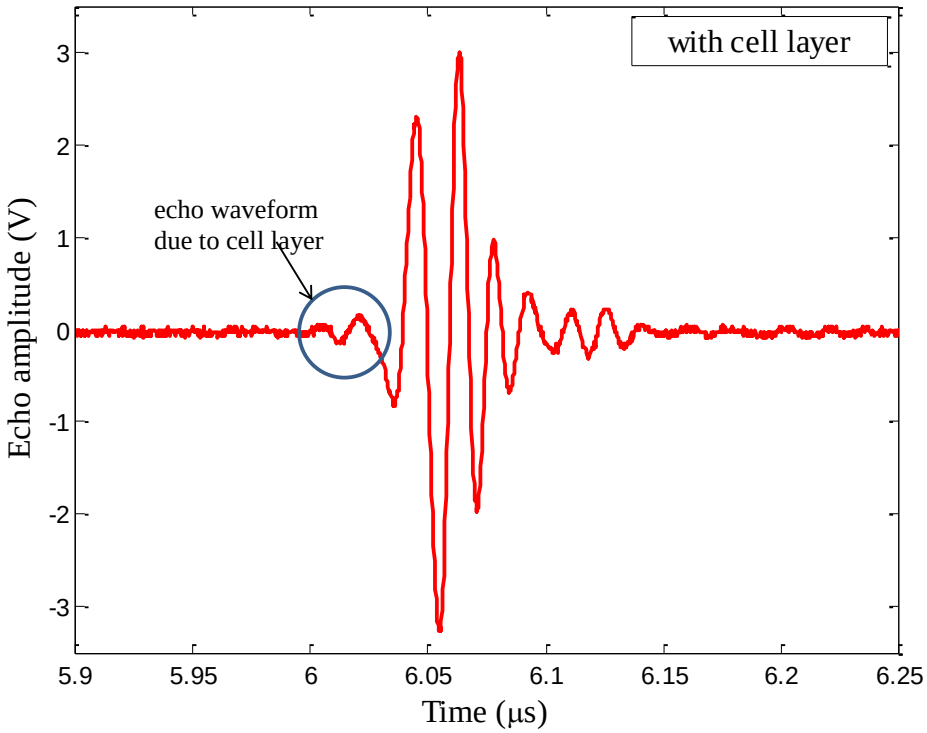

Figure 20: Waveform of wave reflected from cell layer grown on top of the polystyrene substrate

The shift in the time scale for the two waveforms is due to the inconsistency in the thickness of the polystyrene culture dishes used. Two different dishes were used to get these waveforms, which gives a shift of 0.015 μs on the time scale, which corresponds to a thickness difference of 23 μm.

The spectra of the waveforms in Figure 19 and Figure 20 are shown in Figure 21. Each spectrum has a spread from 30 MHz to 80 MHz, and has a central frequency of 60 MHz. The maximum intensity is seen at this frequency, and the spectrum was normalized by this amplitude for each corresponding spectrum. However, it can be seen that it is extremely difficult to determine the minimum and maximum points on either of these spectra, which are required to estimate the phase angles Φ_{front} and Φ_{back}, as specified in equations (19) and (20). Thereby, it is not possible to determine the cell layer thickness and sound speed by this approach alone.

It is much easier to proceed if the intensity spectrum for the cell layer is normalized by the reference spectrum. The reference spectrum is the intensity spectrum for the polystyrene substrate, as shown in Figure 21.a.

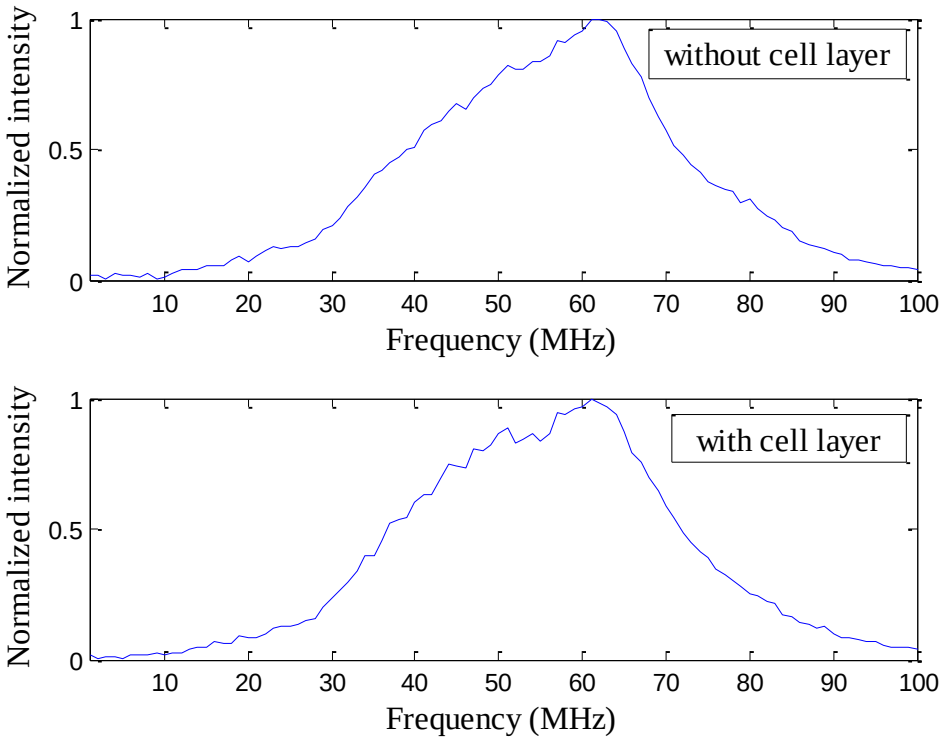

Figure 21: Intensity spectrum of acoustic waves reflected from (a) polystyrene substrate without presence of cells; and (b) cell layer grown on top of the polystyrene substrate

The normalized intensity and phase spectra were Fourier transformed. The MATLAB program for this process is shown in Appendix II. Figure 22 shows a plot of the normalized intensity spectrum. From the Fourier transformed data, the frequencies for the maximum and minimum intensities closest to the central frequency of 60 MHz were used to determine the phase angles for the corresponding frequency. These values and the value for c_0 are used in equations. (19) and (20) to give us the thickness and sound speed in the cell layer. The results are shown in Table 6.

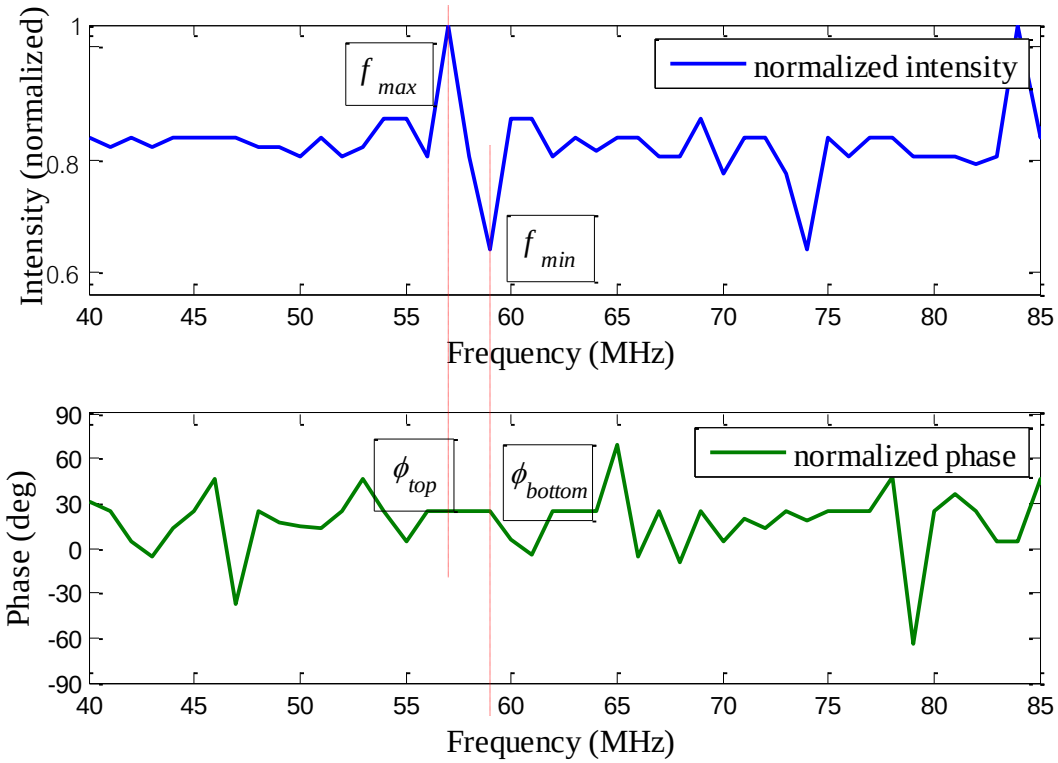

Figure 22: Intensity and phase of the waveform reflected from the layer of differentiating cells at day 14 normalized with the waveform obtained from the reflection from the polystyrene substrate

Table 6: Cell properties measured by pulse-echo test

	Sound speed in medium (m/s)	**Sound speed in cells (m/s)**	**Measured cell thickness (μm)**	**Acoustic impedance of hASC (MRayl)**
Day 1	~ 1531	~ 1557	16.21	1.57
Day 14		~ 1583	16.49	2.13

The measured cell layer thickness and sound velocity values are used to calculate the cell acoustic impedance, which is used in the simulation model. The change in the transducer electrical impedance for hASC samples in the ODM was modeled. PMN-PT resonator dimensions used in the simulation are the same as those experimentally measured (10 mm × 10 mm × 0.45 mm). Cell density values approximated from those presented in previously published references [71, 74] were used as inputs to the model.

4.5 Validation from Simulation

The modeled behavior for a loaded resonator is shown in Figure 23 .The calculated resonator impedance difference for the differentiating and the non-differentiating cells is shown in Table 7. The difference is between simulated values for day 1 and day 14 at resonance and anti-resonance frequencies.

Table 7: Resonator electrical impedance values calculated from the simulation model

	Osteogenic differentiating sample (ODM)		**Non-differentiating sample (CGM)**	
Impedance change (%) $(\frac{Z_{sample} - Z_{medium}}{Z_{medium}})$	**At resonance frequency**	**At anti-resonance frequency**	**At resonance frequency**	**At anti-resonance frequency**
	19.17	-3.56	5.28	-1.3

The simulation model gives a resonance frequency of 4.1 MHz and an anti-resonance frequency of 5.2 MHz. These values match very closely to those observed from the experimental results.

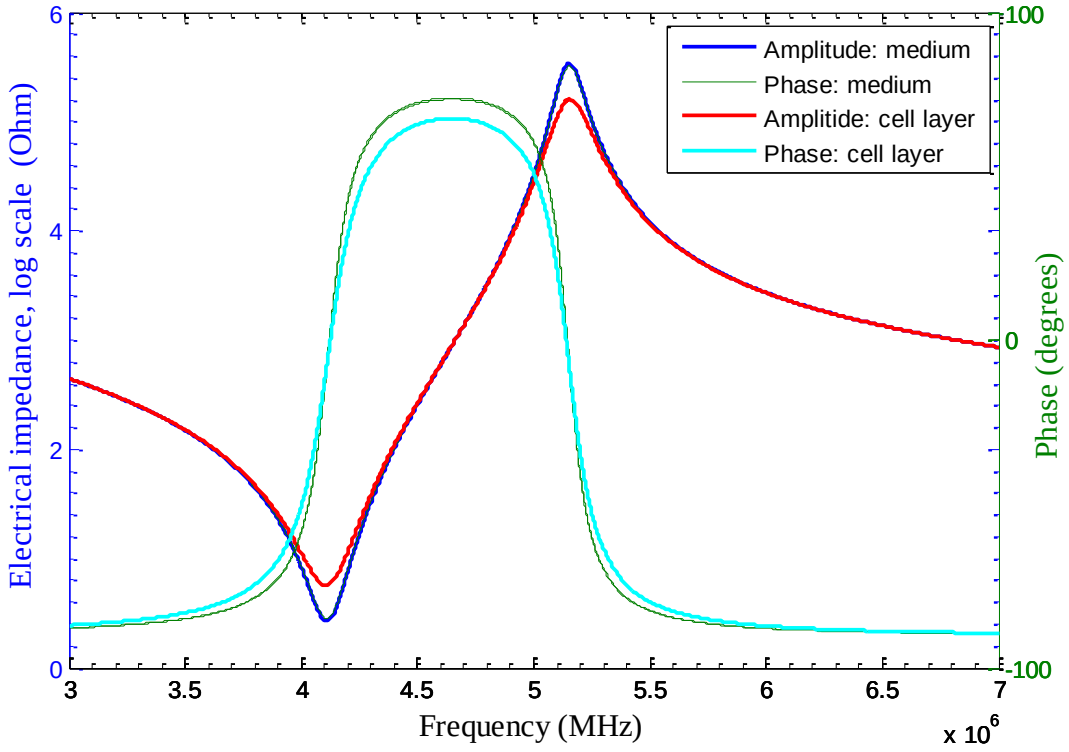

Figure 23: Modeled resonator behavior using Mason's equivalent circuit

A simulation run was conducted for a high frequency (HF) PMN-PT resonator. The calculated frequency for this resonator was 50 MHz. the frequency of a transducer is inversely proportional to the thickness of the piezoelectric element used. For the desired operating frequency of 50 MHz, the resonator thickness was required to be 0.045 mm. the resonator cross-section needs to be reduced in order to minimize the electrode impedance. The calculated electrical impedances based on this mathematical simulation are given in Table 8.

Table 8: Resonator electrical impedance values calculated from the HF simulation model

	Osteogenic differentiating sample (ODM)		Non-differentiating sample (CGM)	
Impedance change (%) $(\frac{Z_{sample} - Z_{medium}}{Z_{medium}})$	**At resonance frequency**	**At anti-resonance frequency**	**At resonance frequency**	**At anti-resonance frequency**
	39.1	-8.03	14.59	-3.96

4.6 Comparison of Measured and Calculated Impedance

The change in the resonator electrical impedance was the key parameter in this research work. This was measured from the experiment and was further validated by a simulation model. A comparison of the observed data with simulated results for the differentiating cells is presented as Table 9.

Table 9: Comparison of observed and calculated resonator electrical impedance for the differentiating sample

	Experimental data	LF simulation	HF simulation
Impedance change	31.7 %	19.17 %	39.1 %

A difference of 12% can be observed between the measured and simulated results for a resonator of frequency 5 MHz. The modeled resonator behavior neglects attenuation losses in the medium and cell layer. Also, cell density values were approximated from earlier published results and were thereby not accurate. The cell growth medium showed a highly attenuating effect, and this was not considered in the simulation. Even in light of this difference between simulated and experimental results we can still conclude that the Mason's equivalent circuit model is valid. From Figure 23, we can see that the introduction of a cell layer causes a change in the resonator electric impedance at both frequency points. A similar observation can be made from the measured resonator response to the change in cell property under osteogenic differentiation.

Figure 12 shows a drop in the measured electrical impedance for the resonator for the stem cells growing in ODM. Thus, we can say that the simulation model can predict the observed electrical impedance change in the piezoelectric transducer.

Based on the calculated values, the change in the resonator electrical impedance for the differentiating cells from day 1 to day 14 was predicted to be 39.1% for a 50 MHz resonator. This shows almost twice the percent change as compared to the simulated result at lower frequency. It has been shown that better image resolution can be achieved using ultrasonic transducers of higher frequencies. We can expect the same for quantitative impedance measurement. It can thus be concluded that higher resonator sensitivity can be achieved at higher frequencies.

Chapter 5

SUMMARY AND FUTURE SCOPE

An innovative, minimally invasive technique was developed for monitoring cell growth and differentiation. Modeling and experimental results show that it is possible to measure change in cell growth by monitoring the electrical impedance change of a resonator.

Cell impedance change was tracked for cell samples undergoing osteogenic differentiation induced by the addition of suitable chemical agents. This was compared with the cell impedance change demonstrated by the non-differentiating batch of cells that were seeded at the same time as the differentiation batch. The cell acoustic impedance was tracked as a function of the electric impedance of a piezoelectric transducer. The cells were grown on a piezoelectric resonator, and the resonator electric impedance was measured using a precision impedance analyzer. The differentiating cell sample showed a change of 31.7% in the electric impedance of the PMN-PT resonator. The corresponding change for the non-differentiating cells was 13.46%.

The main reason for the small change in the impedance value can be attributed to the ‘degree of differentiation’, as shown by the histological examination of the cells. The cells were stained to show areas of calcium deposition. From the images taken using a microscope, it was observed that calcium accretion was not significant. The cell layer properties change due to the change in the mechanical properties, namely the density and speed of sound. The density for the non-differentiating cells is very close to that of the growth medium, and is therefore highly dependent on the amount of calcium accretion. Also, the sound speed changes only with the accretion of calcium. It can be expected that the resonator electric impedance will show a more promising change if more calcium formation occurs. Tracking the cells for a few more days might be a better solution.

A simulation program was developed in MATLAB to validate the observed electrical impedance change. The program was based on Mason's equivalent circuit theory, which is commonly used for the mathematical design and study of ultrasonic transducers. A pulse-echo experiment was carried out to obtain the cell layer thickness and the speed of sound in this layer. These were the required input parameters in the mathematical model. The pulse-echo experiment was carried out in the time-domain, and then the obtained data was Fourier transformed to carry out more accurate analysis. The calculated thickness change in the cell layer over a period of 14 days was around 0.30 μm. The change in the sound velocity in the cell layer was from 1557 m/s on day 1, to 1583 m/s on day 14. These values were used in the MATLAB program and the calculated change in the resonator electric impedance for the differentiating cells was 19.17%.

Although the simulation did not give exact impedance values obtained from the experiment, it showed similar resonator behavior. The measured electrical impedance for the PMN-PT transducer increased with cell-differentiation at the resonant frequency, and dropped at the anti-resonant frequency. The exact observation was made from the simulation. The mathematical model neglected attenuation of sound in the coupling fluid, which in this case, was the cell growth medium. Calibration tests in the growth medium showed that it had a highly attenuating behavior. The attenuation in the cell layer was also neglected. Also, the cell layer thickness is extremely small, around 10 μm, and the Mason model does not work very well for such small dimensions.

The particular usefulness of this technique is that it relies on an intrinsic contrast mechanism and can be used without chemical staining, making it minimally invasive. Cell mechanical properties can be measured in a real-time fashion without having a complicated control system. The cells are not affected physically and are maintained in the growth medium throughout the process, eliminating damage due to contamination or thermal or physical shock due to exposure.

While still in its early stages, this technique may revolutionize the process of cell characterization as it allows for the monitoring of a large population of cells in a real time and high-throughput fashion. Additionally, simulation results shown in this work suggest that resonators with higher resonant frequencies can achieve greater sensitivity in detecting a change in the load acoustic impedance for the same cell thickness and sound speed. Ultimately, a lab-on-chip device could be constructed to act as the goal would be to develop a non-contact transducer-like device that can be used for in vivo characterization of cells in a real-time, throughput manner.

BIBLIOGRAPHY

[1] Tuan RS, Boland G, Tuli R: **Adult mesenchymal stem cells and cell-based tissue engineering**. *Arthritis Research & Therapy* 2003, **5**(1):32-45.

[2] Zuk PA, Zhu M, Mizuno H, Huang J, Futrell JW, Katz AJ, Benhaim P, Lorenz HP, Hedrick MH: **Multilineage cells from human adipose tissue: Implications for cell-based therapies**. *Tissue Engineering* 2001, **7**(2):211-228.

[3] Arvidson K, Abdallah BM, Applegate LA, Baldini N, Cenni E, Gomez-Barrena E, Granchi D, Kassem M, Konttinen YT, Mustafa K *et al*: **Bone regeneration and stem cells**. *Journal of Cellular and Molecular Medicine* 2011, **15**(4):718-746.

[4] Awad HA, Butler DL, Harris MT, Ibrahim RE, Wu Y, Young RG, Kadiyala S, Boivin GP: **In vitro characterization of mesenchymal stem cell-seeded collagen scaffolds for tendon repair: Effects of initial seeding density on contraction kinetics**. *Journal of Biomedical Materials Research* 2000, **51**(2):233-240.

[5] Bao G, Suresh S: **Cell and molecular mechanics of biological materials**. *Nature Materials* 2003, **2**(11):715-725.

[6] Ofek G, Willard VP, Koay EJ, Hu JC, Lin P, Athanasiou KA: **Mechanical Characterization of Differentiated Human Embryonic Stem Cells**. *J Biomech Eng-Trans ASME* 2009, **131**(6).

[7] Chen WLK, Simmons CA: **Lessons from (patho)physiological tissue stiffness and their implications for drug screening, drug delivery and regenerative medicine**. *Adv Drug Deliv Rev* 2011, **63**(4-5):269-276.

[8] Suresh S, Spatz J, Mills JP, Micoulet A, Dao M, Lim CT, Beil M, Seufferlein T: **Connections between single-cell biomechanics and human disease states: gastrointestinal cancer and malaria**. *Acta Biomaterialia* 2005, **1**(1):15-30.

[9] Boyd NF, Martin LJ, Stone J, Greenberg C, Minkin S, Yaffe MJ: **Mammographic densities as a marker of human breast cancer risk and their use in chemoprevention**. *Current oncology reports* 2001, **3**(4):314-321.

[10] Moraes C, Simmons CA, Sun Y: **Cell Mechanics Meets MEMS**. *CSME Bulletin SCGM* 2006:15-18.

[11] Pawley J: **Handbook of Biological Confocal Microscopy**, Third edn: Springer; 2006.

[12] Brand S, Czarnota GJ, Kolios MC, Weiss EC, Lemor R, Ieee: **Visualization of apoptotic cells using scanning acoustic microscopy and high frequency ultrasound**. *2005 IEEE Ultrasonics Symposium, Vols 1-4* 2005:882-885.

[13] Raum K, Reißhauer J, Brandt J: **Frequency and resolution dependence of the anisotropic impedance estimation in cortical bone using time-resolved scanning acoustic microscopy**. *Journal of Biomedical Materials Research Part A* 2004, **71A**(3):430-438.

[14] Brand S, Weiss EC, Lemor RM, Kolios MC: **High frequency ultrasound tissue characterization and acoustic microscopy of intracellular changes**. *Ultrasound in Medicine and Biology* 2008, **34**(9):1396-1407.

[15] Miyasaka C, Tittmann BR: **Imaging and quantitative data acquisition of thinly and thickly sliced biological tissues with scanning acoustic microscopy**. In: *Acoustical Imaging, Vol 27*. Edited by Arnold WKHS, vol. 27; 2004: 591-599.

[16] Hasegawa K, Turner CH, Recker RR, Wu E, Burr DB: **Elastic Properties of Osteoporotic Bone Measured by Scanning Acoustic Microscopy**. *Bone* 1995, **16**(1):85-90.

[17] Brandt J, Franke A, Raum K: **Acoustic microscopy for detection of osteoporotic bone properties**. In*: 2004*: IEEE; 2004: 573-575 Vol. 571.

[18] Raum K, Jenderka KV, Klemenz A, Brandt J: **Multilayer analysis: quantitative scanning acoustic microscopy for tissue characterization at a microscopic scale**. *Ultrasonics, Ferroelectrics and Frequency Control, IEEE Transactions on* 2003, **50**(5):507-516.

[19] Raum K, Brandt J, Klemenz A, Cobet U: **Quantitative scanning acoustic microscopy for the determination of the elastic properties of cortical bone**. *Z Med Phys* 1999, **9**:246–253.

[20] Raum K, Cobet U, Smitmans L, Brandt J: **Quantitative scanning acoustic microscopy investigation of cortical bone using a multilayer analysis method**. In*: 1999*: IEEE; 1999: 593-596 vol. 591.

[21] Brandt J, Klemenz A, Raum K, Seidler S: **Scanning Acoustic Microscopy for Micromeasurement of Elastomechanical Bone Properties-Comparison with Nanoindentation Results**. *ACOUSTICAL IMAGING* 2002, **26**:53-60.

[22] Leguerney I, Raum K, Saïed A, Follet H, Boivin G, Brandt J, Laugier P: **Trabecular bone properties evaluated by scanning acoustic microscopy**. *Proceedings WCU* 2003:295-298.

[23] Daft CMW, Briggs GAD: **Widebang Acoustic Microscopy of Tissue**. *Ieee Transactions on Ultrasonics Ferroelectrics and Frequency Control* 1989, **36**(2):258-263.

[24] Daft CMW, Briggs GAD: **Tissue Characterization with Microscopic Resolution**. *Ieee Transactions on Ultrasonics Ferroelectrics and Frequency Control* 1987, **34**(3):406-406.

[25] Daft CMW, Briggs GAD: **The Elastic Microstructure of Various Tissues**. *Journal of the Acoustical Society of America* 1989, **85**(1):416-422.

[26] Daft C, Briggs G, O'Brien Jr W: **Frequency dependence of tissue attenuation measured by acoustic microscopy**. In*: 1989*: IEEE; 1989: 971-974 vol. 972.

[27] Luers H, Hillmann K, Litniewski J, Bereiterhahn J: **Acoustic Microscopy of Cultured Cells - Distribution of Forces and Cytoskeletal Elements**. *Cell Biophysics* 1991, **18**(3):279-293.

[28] Strohm EM, Kolios MC, Ieee: **Measuring the Mechanical Properties of Cells using Acoustic Microscopy**; 2009.

[29] Weiss EC, Anastasiadis P, Pilarczyk G, Lemor RM, Zinin PV: **Mechanical properties of single cells by high-frequency time-resolved acoustic Microscopy**. *Ieee Transactions on Ultrasonics Ferroelectrics and Frequency Control* 2007, **54**(11):2257-2271.

[30] Bost W, Stracke F, Weiss EC, Narasimhan S, Kolios MC, Lemor R: **High frequency optoacoustic microscopy**. *Conference proceedings : Annual International Conference of the IEEE Engineering in Medicine and Biology Society IEEE Engineering in Medicine and Biology Society Conference* 2009, **2009**:5883-5886.

[31] Rui M, Narashimhan S, Bost W, Stracke F, Weiss E, Lemor R, Kolios MC: **Gigahertz optoacoustic imaging for cellular imaging**. In: *Photons Plus Ultrasound: Imaging and Sensing 2010.* Edited by Oraevsky AAWLV, vol. 7564; 2010.

[32] Schenkl S, Weiss E, Stark M, Stracke F, Riemann I, Lemor R, Konig K: **Imaging living cells with a combined high-resolution multi-photon-acoustic microscope - art. no. 64372A**. *Photons Plus Ultrasound: Imaging and Sensing 2007* 2007, **6437**:A4372-A4372.

[33] Schenkl S, Weiss EC, Stracke F, Saijer D, Stark M, Riemann I, Lemor RM, Konig K: **In-vivo observation of cells with a combined high-resolution multiphoton-acoustic scanning microscope**. *Microscopy Research and Technique* 2007, **70**(5):476-480.

[34] Foster FS, Pavlin CJ, Harasiewicz KA, Christopher DA, Turnbull DH: **Advances in ultrasound biomicroscopy**. *Ultrasound in Medicine and Biology* 2000, **26**(1):1-27.

[35] Saijo Y, Hozumi N, Kobayashi K, Okada N, Ishiguro T, Hagiwara Y, Filho EdS, Yambe T, Ieee: **Ultrasound speed and impedance microscopy for in vivo imaging**. In: *2007 Annual International Conference of the Ieee Engineering in Medicine and Biology Society, Vols 1-16.* 2007: 1350-1353.

[36] Shishitani T, Yoshizawa S, Umemura SI: **Change in acoustic impedance and sound speed of HIFU-exposed chicken breast muscle**. In: *Ultrasonics Symposium (IUS), 2010 IEEE: 11-14 Oct. 2010 2010*; 2010: 1384-1387.

[37] Nakano A, Uemura T, Hozumi N, Nagao M, Yoshida S, Kobayashi K, Yamamoto S, Saijo Y: **Non-contact observation of cultured cells by acoustic impedance microscope**. In: *Ultrasonics Symposium, 2008 IUS 2008 IEEE: 2-5 Nov. 2008 2008*; 2008: 1893-1896.

[38] Raum K, Cleveland RO, Peyrin F, Laugier P: **Derivation of elastic stiffness from site-matched mineral density and acoustic impedance maps**. *Physics in Medicine and Biology* 2006, **51**:747.

[39] Brandao MM, Fontes A, Cesar CL, Costa FF, Saad STO, Barjas-Castro ML: **Deformability of stored as red blood cell units measured by optical tweezers**. *Blood* 2001, **98**(11):103B-103B.

[40] Guck J, Ananthakrishnan R, Moon TJ, Cunningham CC, Käs J: **Optical Deformability of Soft Biological Dielectrics**. *Physical Review Letters* 2000, **84**(23):5451-5454.

[41] F.G M: **Acoustic radiation force on a sphere in standing and quasi-standing zero-order Bessel beam tweezers**. *Annals of Physics* 2008, **323**(7):1604-1620.

[42] Huang H, Kamm RD, Lee RT: **Cell mechanics and mechanotransduction: pathways, probes, and physiology**. *American Journal of Physiology-Cell Physiology* 2004, **287**(1):C1-C11.

[43] Van Vliet KJ, Bao G, Suresh S: **The biomechanics toolbox: experimental approaches for living cells and biomolecules**. *Acta Materialia* 2003, **51**(19):5881-5905.

[44] A-Hassan E, Heinz WF, Antonik MD, D'Costa NP, Nageswaran S, Schoenenberger C-A, Hoh JH: **Relative Microelastic Mapping of Living Cells by Atomic Force Microscopy**. *Biophysical Journal* 1998, **74**(3):1564-1578.

[45] Eric H: **Imaging of living cells by atomic force microscopy**. *Progress in Surface Science* 1994, **46**(1):39-60.

[46] Schaus SS, Henderson ER: **Cell viability and probe-cell membrane interactions of XR1 glial cells imaged by atomic force microscopy**. *Biophysical Journal* 1997, **73**(3):1205-1214.

[47] Hoh JH, Schoenenberger CA: **Surface morphology and mechanical properties of MDCK monolayers by atomic force microscopy**. *Journal of Cell Science* 1994, **107**(5):1105-1114.

[48] Butt HJ, Wolff EK, Gould SAC, Dixon Northern B, Peterson CM, Hansma PK: **Imaging cells with the atomic force microscope**. *Journal of Structural Biology*, **105**(1-3):54-61.

[49] Radmacher M: **Measuring the elastic properties of biological samples with the AFM**. *Ieee Engineering in Medicine and Biology Magazine* 1997, **16**(2):47-57.

[50] Hayashi K: **Tensile properties and local stiffness of cells**. *Mechanics of biological tissue* 2006:137.

[51] Tao N, Lindsay S, Lees S: **Measuring the microelastic properties of biological material**. *Biophysical Journal* 1992, **63**(4):1165-1169.

[52] Radmacher M, Fritz M, Kacher CM, Cleveland JP, Hansma PK: **Measuring the viscoelastic properties of human platelets with the atomic force microscope**. *Biophysical Journal* 1996, **70**(1):556-567.

[53] Braet, Seynaeve, De Z, Wisse: **Imaging surface and submembranous structures with the atomic force microscope: a study on living cancer cells, fibroblasts and macrophages**. *Journal of Microscopy* 1998, **190**(3):328-338.

[54] Zhang G, Long M, Wu ZZ, Yu WQ: **Mechanical properties of hepatocellular carcinoma cells**. *World Journal of Gastroenterology* 2002, **8**(2):243-246.

[55] Beil M, Micoulet A, von Wichert G, Paschke S, Walther P, Omary MB, Van Veldhoven PP, Gern U, Wolff-Hieber E, Eggermann J *et al*: **Sphingosylphosphorylcholine regulates keratin network architecture and visco-elastic properties of human cancer cells**. *Nature Cell Biology* 2003, **5**(9):803-811.

[56] Puig-de-Morales M, Grabulosa M, Alcaraz J, Mullol J, Maksym GN, Fredberg JJ, Navajas D: **Measurement of cell microrheology by magnetic twisting cytometry with frequency domain demodulation**. *Journal of Applied Physiology* 2001, **91**(3):1152-1159.

[57] Kosawada T, Konno K-i, Yamamura S, Kanazawa T: **Piezo micro probe sensor system to detect environmental stresses induced in living cells and tissues**. *Microsystem Technologies* 2005, **11**(8):943-949.

[58] Murayama Y, Constantinou CE, Omata S: **Micro-mechanical sensing platform for the characterization of the elastic properties of the ovum via uniaxial measurement**. *Journal of Biomechanics* 2004, **37**(1):67-72.

[59] Tan JL, Tien J, Pirone DM, Gray DS, Bhadriraju K, Chen CS: **Cells lying on a bed of microneedles: An approach to isolate mechanical force**. *Proceedings of the National Academy of Sciences of the United States of America* 2003, **100**(4):1484-1489.

[60] Lemmon CA, Sniadecki NJ, Ruiz SA, Tan JL, Romer LH, Chen CS: **Shear force at the cell-matrix interface: enhanced analysis for microfabricated post array detectors**. *Mechanics & chemistry of biosystems : MCB* 2005, **2**(1):1-16.

[61] Liu Z, Sniadecki NJ, Chen CS: **Mechanical Forces in Endothelial Cells during Firm Adhesion and Early Transmigration of Human Monocytes**. *Cellular and Molecular Bioengineering* 2010, **3**(1):50-59.

[62] Li B, Xie L, Starr ZC, Yang Z, Lin J-S, Wang JHC: **Development of micropost force sensor array with culture experiments for determination of cell traction forces**. *Cell Motility and the Cytoskeleton* 2007, **64**(7):509-518.

[63] Cobbold RSC: **Foundations of biomedical ultrasound**: Oxford University Press, USA; 2007.

[64] Mason WP: **Electromechanical transducers and wave filters**: Van Nostrand Reinhold; 1946.

[65] Sherrit S, Olazabal V, Sansinena JM, Bao X, Chang Z, Bar-Cohen Y: **The use of piezoelectric resonators for the characterization of mechanical properties of polymers**. In*: 2002*: Citeseer; 2002.

[66] Sherrit S, Mukherjee BK: **Characterization of Piezoelectric Materials for Transducers**. *Arxiv preprint arXiv:07112657* 2007.

[67] Sherar M, Foster F: **The design and fabrication of high frequency poly (vinylidene fluoride) transducers**. *Ultrasonic imaging* 1989, **11**(2):75-94.

[68] LifeTechnologies: **Invitrogen™**.

[69] Filiâtre C, Bardèche G, Valentin M: **Transmission Line Model for Immersed Quartz Crystal Sensors**. *Sensors and Actuators A: Physical* 1994, **44**(2):137-144.

[70] Bagnaninchi PO, Drummond N: **Real-time label-free monitoring of adipose-derived stem cell differentiation with electric cell-substrate impedance sensing**. *Proceedings of the National Academy of Sciences* 2011, **108**(16):6462.

[71] Hachiya H, Ohtsuki S, Tanaka M, Dunn F: **Determination of Sound Speed in Biological Tissues Based on Frequency Analysis of Pulse Response.** *Journal of the Acoustical Society of America* 1992, **92**(3):1564-1568.

[72] Hozumi N, Yamashita R, Lee CK, Nagano M, Kobayashi K, Saijo Y, Tanaka M, Tanaka N, Ohtsuki S: **Ultrasonic sound speed microscope for biological tissue characterization driven by nanosecond pulse**. In: *Acoustical Imaging, Vol 27.* Edited by Arnold WKHS, vol. 27; 2004: 495-501.

[73] Hozumi N, Yamashita R, Lee CK, Nagao M, Kobayashi K, Saijo Y, Tanaka M, Tanaka N, Ohtsuki S: **Time–frequency analysis for pulse driven ultrasonic microscopy for biological tissue characterization**. *Ultrasonics* 2004, **42**(1-9):717-722.

[74] Juopperi TA, Schuler W, Yuan X, Collector MI, Dang CV, Sharkis SJ: **Isolation of Bone Marrow–Derived Stem Cells using Density-Gradient Separation**. *Experimental Hematology* 2007, **35**(2):335-341.

[75] Bakshi S, Williams J, Matthieu P, Loboa E, Jiang X: **Cell Characterization Using High Frequency Ultrasound.** *IEEE Ultrasonics Symposium 2011: 18-21 Oct*

APPENDICES

Appendix I: Matlab Program for Impedance Calculation

```
clc
clear all
close all

%% Piezoelectric element properties (PMN-PT)

% low frequency resonator
deltaf = 8000;     % step size
maxf = 7e6;        % minimum frequency (Hz)
minf = 3e6;        % maximum frequency (Hz)
maxk = ((maxf-minf)/deltaf)+1;
maxn = 5;          % number of loading layers
minZ = 0;
maxZ = 1e3;
% element dimensions
l = 0.450e-3;      % element thickness (m)
L = 10e-3;         % element diameter/length (m)
A = L*L;           % cross sectional area (m^2)

% % high frequency resonator
% deltaf = 8000;     % step size
% maxf = 70e6;       % minimum frequency (Hz)
% minf = 30e6;       % maximum frequency (Hz)
% maxk = ((maxf-minf)/deltaf)+1;
% maxn = 5;          % number of loading layers
% minZ = 0;
% maxZ = 1e3;
% % element dimensions
% l = 0.0450e-3;     % element thickness (m)
% L = 2e-3;          % element diameter/length (m)
% A = L*L;           % cross sectional area (m^2)

% material properties
rho = 8100;        % density (kg/m^3)
c33 = 174e9;       % elastic stiffness (N/m^2)
epsilon0 = 8.854e-12;       % vacuum permittivity (c/V-m)
epsilonS = epsilon0.*800;   % clamped permittivity of medium (c/V-m)
v = sqrt(c33/rho)          % stiffened compressional speed (m/s)
f0 = v/(2*l)       % antiresonance frequency (Hz)
kt = 0.64;         % coupling coefficient

% calculated properties
lambda = v/f0;     % wavelength
omega0 = 2.*pi.*f0; % angular frequency of transducer
C0 = A.*epsilonS./l;% clamped capacitance
Z0 = rho.*v;       % characteristic acoustic impedance of element
Za = A.*Z0;        % specific acoustic impedance of element
h = kt.*sqrt(c33./epsilonS);      %
N = C0.*h;         % turns ratio of transformer
```

```
%% Model calculations (for load impedances = 1 to 'n' MRayl)

for k = 1:maxk
   f(k)= minf+deltaf*(k-1);
   omega(k) = 2*pi*f(k);

   % unloaded transducer acoustic loads
   tau(k) = omega(k)/v;
   Zt(k) = i*Za*tan(tau(k)*l/2);
   Zs(k) = -i*Za*csc(tau(k)*l);
   a(k) = pi*omega(k)/omega0;
   Zc(k) = 1/(i*omega(k)*C0);
   Zel_unloaded(k) = Zc(k)*(1-((kt^2)*tan(a(k)/2)/(a(k)/2)));

   % electrical impedance(measured at electrical port)
   Z(k) = Zs(k) + Zt(k)/2;
   Zel_loaded(k) = Zc(k)*(1 - Zc(k)*(N^2)/Z(k));

   for n = 1:maxn
      Zl(n) = (n-0.996)*10^6*A;
      Zmech(k,n) = Zs(k) + Zt(k)*(Zt(k)+Zl(n))/(2*Zt(k)+Zl(n));   % total acoustic (mechanical)
impedance
      Zel_total(k,n) = Zc(k)*(1-(Zc(k)*N^2)/Zmech(k,n));        % total electrical impedance
   end
end

for n = 1:maxn
   Zmax(n) = 10;
   for k = 2:maxk

      if Zel_total(k,n) > Zmax(n)
         Zmax(n) = Zel_total(k,n);
         nmax(n) = n;
         fmax(n) = f(k);
      end
   end
end

% display output
fmax
res_imp_unloaded = min(abs(Zel_unloaded))
antires_imp_unloaded = max(abs(Zel_unloaded))
res_imp_loaded = min(abs(Zel_total))
antires_imp_loaded = max(abs(Zel_total))

% % Plots
% figure;
% subplot(2,1,1);
% semilogy(f,abs(Zel_total));
% xlim([minf,maxf]), ylim([minZ,maxZ]);
% title('Electrical impedance vs
```

```
Frequency','FontWeight','bold','FontWeight','bold','FontSize',12,'FontAngle','italic');
% xlabel('Frequency (Hz)'), ylabel(['Electrical impedance',sprintf('\n'),'- loaded (Ohm)']);
%
% subplot(2,1,2);
% semilogy(f,abs(Zel_unloaded), 'color', 'red');
% xlim([minf,maxf]), ylim([minZ,maxZ]);
% title('Electrical impedance vs Frequency','FontWeight','bold','FontSize',12,'FontAngle','italic');
% xlabel('Frequency (Hz)'), ylabel(['Electrical impedance',sprintf('\n'),'- unloaded (Ohm)']);

%% Layered model

% layer1: epoxy + tungsten = backing layer
l1 = 20e-3;   % thickness (m)
A1 = 0;       % cross sectional area (m^2)
rho1 = 1000;  % density (kg/m^3)
v1 = 1480;    % longitudinal wave velocity in medium (m/s)
Z1 = A1*rho1*v1% acoustic impedance of layer 1
for k = 1:maxk
   tau1(k) = omega(k)/v1;
end

% layer2: gold electrode
l2 = 350e-10;  % thickness (m)
A2 = A;       % cross sectional area (m^2)
rho2 = 19700;  % density (kg/m^3)
v2 = 3240;     % longitudinal wave velocity in medium (m/s)
Z2 = A2*rho2*v2 % acoustic impedance of layer 2
for k = 1:maxk
   tau2(k) = omega(k)/v2;
end

% layer3: coupling fuid - top
l3 = 20e-3;    % thickness (m)
A3 = A;       % cross sectional area (m^2)
rho3 = 1200;   % density (kg/m^3)
v3 = 1490;     % longitudinal wave velocity in medium (m/s)
Z3 = A3*rho3*v3 % acoustic impedance of layer 3
for k = 1:maxk
   tau3(k) = omega(k)/v3;
end

% layer4: coupling fuid - bottom
l4 = 20e-3;    % thickness (m)
A4 = A3;       % cross sectional area (m^2)
rho4 = rho3;   % density (kg/m^3)
v4 = v3;     % longitudinal wave velocity in medium (m/s)
Z4 = A4*rho4*v4 % acoustic impedance of layer 3
for k = 1:maxk
   tau4(k) = tau3(k);
end
```

```
% layer5: cell layer
l5 = 16.49e-6;   % thickness (m)
A5 = 0/5;        % cross sectional area (m^2)
rho5 = 1350;   % density (kg/m^3)
v5 = 1583;     % longitudinal wave velocity in medium (m/s)
Z5 = A5*rho5*v5 % acoustic impedance of layer 2
for k = 1:maxk
   tau5(k) = omega(k)/v5;
end

%% Model calculations

for k = 1:maxk
%    Zl_1t(k) = i*Z1*tan(tau1(k)*l1/2);
%    Zl_1s(k) = -i*Z1*csc(tau1(k)*l1);
%    Zl_1(k) = (Zl_1t(k))/2 + Zl_1s(k);
   Zl_1(k) = abs(i*Z1*tan(tau1(k)*l1/2));
%    Zl_1(k) = abs(i*rho1*v1*(tau1(k)*l1));
%    Zl_1(k) = 1.48e6*A1;

%    Zl_2t(k) = i*Z2*tan(tau2(k)*l2/2);
%    Zl_2s(k) = -i*Z2*csc(tau2(k)*l2);
%    Zl_2(k) = Zl_2t(k)/2 + Zl_2s(k);
   Zl_2(k) = abs(i*Z2*tan(tau2(k)*l2/1));
%    Zl_2(k) = abs(i*rho2*v2*(tau2(k)*l2));
%    Zl_2(k) = 62.6e6*A2;

%    Zl_3t(k) = i*Z3*tan(tau3(k)*l3/2);
%    Zl_3s(k) = -i*Z3*csc(tau3(k)*l3);
%    Zl_3(k) = Zl_3t(k)/2 + Zl_3s(k);
   Zl_3(k) = abs(i*Z3*tan(tau3(k)*l3/1));
%    Zl_3(k) = abs(i*rho3*v3*(tau3(k)*l3));
%    Zl_3(k) = 1.48e6*A3;

%    Zl_4t(k) = i*Z4*tan(tau4(k)*l4/2);
%    Zl_4s(k) = -i*Z4*csc(tau4(k)*l4);
%    Zl_4(k) = Zl_4t(k)/2 + Zl_4s(k);
   Zl_4(k) = abs(i*Z4*tan(tau4(k)*l4/1));
%    Zl_4(k) = abs(i*rho4*v4*(tau4(k)*l4));
%    Zl_4(k) = 1.48e6*A4;

%    Zl_5t(k) = i*Z5*tan(tau5(k)*l5/2);
%    Zl_5s(k) = -i*Z5*csc(tau5(k)*l5);
%    Zl_5(k) = Zl_5t(k)/2 + Zl_5s(k);
   Zl_5(k) = abs(i*Z5*tan(tau5(k)*l5/1));
%    Zl_5(k) = abs(i*rho5*v5*(tau5(k)*l5));
%    Zl_5(k) = 1.48e6*A5;

%    Zl_total(k) = 1/(1/Zl_1(k) + 1/Zl_2(k) + 1/Zl_3(k) + 1/Zl_4(k));
   Zl_total(k) = Zl_1(k) + 2*Zl_2(k) + Zl_3(k) + Zl_4(k) + Zl_5(k);
```

```
   % Complete model: PZT-5H + Layer1
   Zmech(k,n) = Zs(k) + Zt(k)*(Zt(k)+Zl(n))/(2*Zt(k)+Zl(n));              % total acoustic (mechanical)
impedance
   Zel_total(k,n) = Zc(k)*(1-(Zc(k)*N^2)/Zmech(k,n));
   Zmech_layered(k) = Zs(k) + Zt(k)*(Zt(k)+Zl_total(k))/(2*Zt(k)+Zl_total(k)); % total acoustic
(mechanical) impedance
   Zel_total_layered(k) = Zc(k)*(1-(Zc(k)*N^2)/Zmech_layered(k));          % total electrical impedance
end

% display output
res_ac_imp_layer1 = min(abs(Zl_1/A1))
res_ac_imp_layer2 = min(abs(Zl_2))
res_ac_imp_layer3 = min(abs(Zl_3/A3))
res_ac_imp_layers_total = min(abs(Zl_total))
res_imp_layered = min(abs(Zel_total_layered))
antires_imp_layered = max(abs(Zel_total_layered))

% Plots
figure;
% [AX,H1,H2] = plotyy(f,abs(Zel_total_layered),f,angle(Zel_total_layered)*180/pi);
[AX,H1,H2] = plotyy(f,log(abs(Zel_total_layered)),f,angle(Zel_total_layered)*180/pi);
% title('Electrical impedance vs Frequency',...
%    'FontWeight','bold','FontWeight','bold','FontSize',12,'FontAngle','italic');
xlabel('Frequency (Hz)');
set(get(AX(1),'Ylabel'),...
   'String','Electrical impedance (log) - loaded (Ohm)');
set (gca,'YTick',[-10 -8 -6 -4 -2 0 2 4 6 8 10],'YMinorTick','on');
set(get(AX(2),'Ylabel'),'String','Phase (degrees)');
set(gca,'XMinorTick','on','YMinorTick','on');
text(fmax(1),antires_imp_layered,'aaa');
```

Appendix II: Matlab Program for Normalization and FFT of Reflection Waveforms

```
clc
clear all
close all

%% Read file

Uy = xlsread('C:\Users\User\Dropbox\Thesis documents\plots\PE FFT\media.CGM.ODM time-vltg
data.xlsx');
t_media = Uy(:,1);
y_media = Uy(:,2);
t_cells = Uy(:,3);
y_cells = Uy(:,5);

%
t_media = t_media';
y_media = y_media';
t_cells = t_cells';
y_cells = y_cells';

%% Waveform plots

% without cells
figure (1);
plot(t_media,y_media,'b','LineWidth',2);
xlabel('Time ({\mu}s)', 'FontSize',12,'FontName','Times New Roman'),...
   ylabel('Echo amplitude (V)','FontSize',12,'FontName','Times New Roman'),...
   legend('measured echo waveform');
xlim([5.9 6.25]), ylim([-3.5 3.5]);

% with cells
figure (2);
plot(t_media,y_cells,'r','LineWidth',2);
xlabel('Time ({\mu}s)', 'FontSize',12,'FontName','Times New Roman'),...
   ylabel('Echo amplitude (V)','FontSize',12,'FontName','Times New Roman'),...
   legend('measured echo waveform');
xlim([5.9 6.25]), ylim([-3.5 3.5]);

%% FFT

% without cells
delta_media = t_media(2)-t_media(1);
fs_media = 1/delta_media;
N_media = length(y_media);
fy_media = fft(y_media);
f_media = (0:N_media-1)*fs_media/N_media;
```

```
% with cells
delta_cells = t_media(2)-t_media(1);
fs_cells = 1/delta_cells;
N_cells = length(y_cells);
fy_cells = fft(y_cells);
f_cells = (0:N_cells-1)*fs_cells/N_cells;

%% Plots
% media intensity spectrum and phase
figure (3);
subplot(2,1,1);
plot(f_media,abs(fy_media),'LineWidth',1);
xlim([1 100]);
xlabel('Frequency (MHz)','FontSize',12,'FontName','Times New Roman'),...
   ylabel('Intensity spectrum (dB)','FontSize',12,'FontName','Times New Roman'),...
   annotation('textbox',[0.64 0.83 0.24 0.06],...
   'String',{'without cell layer'},'HorizontalAlignment','center',...
   'FontSize',12,'FontName','Times New Roman','FitBoxToText','off');
subplot(2,1,2);
plot (f_media,angle(fy_media)*180/pi,'LineWidth',1);
xlim([1 100]);
xlabel('Freq(MHz)','FontSize',12,'FontName','Times New Roman'),...
   ylabel('Phase (deg)','FontSize',12,'FontName','Times New Roman');

% cell intensity spectrum and phase
figure (4);
subplot(2,1,1);
plot(f_cells,abs(fy_cells),'LineWidth',1);
xlim([1 100]);
xlabel('Frequency (MHz)','FontSize',12,'FontName','Times New Roman'),...
   ylabel('Intensity spectrum (dB)','FontSize',12,'FontName','Times New Roman'),...
   annotation('textbox',[0.64 0.83 0.24 0.06],...
   'String',{'with cell layer'},'HorizontalAlignment','center',...
   'FontSize',12,'FontName','Times New Roman','FitBoxToText','off');
subplot(2,1,2);
plot (f_cells,angle(fy_cells)*180/pi,'LineWidth',1);
xlim([1 100]);
xlabel('Freq(MHz)','FontSize',12,'FontName','Times New Roman'),...
   ylabel('Phase (deg)','FontSize',12,'FontName','Times New Roman');

% comparison of media and cell intensity spectra
figure (5);
subplot(2,1,1);
plot(f_media,abs(fy_media),'LineWidth',1);
xlim([1 100]);
xlabel('Frequency (MHz)','FontSize',12,'FontName','Times New Roman'),...
   ylabel('Intensity spectrum (dB)','FontSize',12,'FontName','Times New Roman'),...
   annotation('textbox',[0.64 0.83 0.24 0.06],...
   'String',{'without cell layer'},'HorizontalAlignment','center',...
   'FontSize',12,'FontName','Times New Roman','FitBoxToText','off');
```

```
subplot(2,1,2);
plot(f_cells,abs(fy_cells),'LineWidth',1);
xlim([1 100]);
xlabel('Frequency (MHz)','FontSize',12,'FontName','Times New Roman'),...
   ylabel('Intensity spectrum (dB)','FontSize',12,'FontName','Times New Roman'),...
   annotation('textbox',[0.65 0.35 0.22 0.06],...
   'String',{'with cell layer'},'HorizontalAlignment','center',...
   'FontSize',12,'FontName','Times New Roman','FitBoxToText','off');

%% Normalization

% intensity spectrum
figure (6);
subplot(2,1,1);
plot(f_media,(abs(y_cells)/abs(y_media)),'LineWidth',10);
xlim([1*10^0 100*10^0]);
xlabel('Frequency (MHz)','FontSize',12,'FontName','Times New Roman'),...
   ylabel('Intensity spectrum (dB)','FontSize',12,'FontName','Times New Roman'),...
% phase
subplot(2,1,2);
plot(f_cells,(angle(fy_cells)/angle(fy_media)),'LineWidth',1);
xlim([1 100]);
xlim([1 100]);
xlabel('Freq(MHz)','FontSize',12,'FontName','Times New Roman'),...
   ylabel('Phase (deg)','FontSize',12,'FontName','Times New Roman');
```